Nanoscale

ROYAL SOCIETY OF CHEMISTRY

REVIEW

View Article Online
View Journal | View Issue

Cite this: *Nanoscale*, 2023, **15**, 5537

Integration of nanomaterial sensing layers on printable organic field effect transistors for highly sensitive and stable biochemical signal conversion

Yawen Song, Wei Tang,* Lei Han, Yan Liu, Chaochao Shen, Xiaokuan Yin, Bang Ouyang, Yuezeng Su* and Xiaojun Guo*

Organic field effect transistor (OFET) devices are one of the most popular candidates for the development of biochemical sensors due to their merits of being flexible and highly customizable for low-cost large-area manufacturing. This review describes the key points in constructing an extended-gate type OFET (EGOFET) biochemical sensor with high sensitivity and stability. The structure and working mechanism of OFET biochemical sensors are described firstly, emphasizing the importance of critical material and device engineering to higher biochemical sensing capabilities. Next, printable materials used to construct sensing electrodes (SEs) with high sensitivity and stability are presented with a focus on novel nanomaterials. Then, methods of obtaining printable OFET devices with steep subthreshold swing (SS) for high transconductance efficiency are introduced. Finally, approaches for the integration of OFETs and SEs to form portable biochemical sensor chips are introduced, followed by several demonstrations of sensory systems. This review will provide guidelines for optimizing the design and manufacturing of OFET biochemical sensors and accelerating the movement of OFET biochemical sensors from the laboratory to the marketplace.

Received 21st October 2022,
Accepted 17th February 2023

DOI: 10.1039/d2nr05863d

rsc.li/nanoscale

1. Introduction

As one of the potential large-area electronic devices, organic field effect transistors (OFETs) have attracted a lot of attention from academia and industry since its proposal in 1986.[1] The exploration of soluble organic semiconductors (OSCs) and gate dielectric materials enables low-cost fabrication of OFETs with diverse structures by solution-based and printing processes.[2–5] Currently, inkjet printing, screen printing, spin coating, blade coating, and roll-to-roll printing technologies have been investigated in the manufacturing of such OFETs, which boost the development of promising printable electronics.[6–10] The feasibility of low-temperature processing also makes it possible to fabricate OFET devices on flexible substrates such as plastic or paper, endowing OFETs with excellent mechanical flexibility and biocompatibility.[11–14] The diversity of OSCs, gate dielectric materials and processes endows OFETs with virtues of cost-effective manufacturing, short design-to-product cycles, and flexible form factors, which are very attractive for developing biochemical sensors in a rapid customized way.

To date, many efforts have been devoted to exploiting the OFET technique for electrochemical sensors in health diagnostics and environmental monitoring applications.[15–19] Meanwhile, depending on the specific stacking of the functional layers, OFET biochemical sensors were constructed in several assembly structures.[15,20–23] Among the widely used OFET electrochemical sensors, the extended-gate type OFET (EGOFET) is still very popular, and is similar to the classic ion-sensitive field effect transistor (ISFET) based on complementary metal oxide semiconductor (CMOS) technology.[24] The utilization of an extended-gate can not only eliminate the stability issue induced by solution leakage but also bring more opportunities for material choices and flexibility of device design. Generally, an EGOFET biochemical sensor consists of a transistor for signal amplification and a sensing electrode (SE) for transducing external biochemical signals to electrical ones, providing a low-cost electronic sensing platform for the construction of various biochemical sensors.[25–28] With the ability to convert small potential signals into large current signals, OFET biochemical sensors can achieve higher sensitivity and signal-to-noise ratios, making them an optimal choice for the analysis of trace biochemicals.[29] Furthermore, designing the sensing interface with different sensitive materials could create different potentiometric sensing systems. In this way, plenty of work has been done for constructing OFET biochemical sensors during the last few decades,[30,31] detecting electrolyte ions (Na^+, K^+, H^+, Ca^{2+}...),[32–34] heavy metal ions (Hg^{2+}, Pb^{2+}, Cd^{2+}...),[18,19] small molecules (glucose, taurine, L-lactate...),[35–37] protein molecules,[38] antibodies/antigens,[15,39] DNA or RNA of pathogens,[29] *etc*.

School of Electronic Information and Electrical Engineering, Shanghai Jiao Tong University, Shanghai 200240, China. E-mail: terry_tang@sjtu.edu.cn, yzsu@sjtu.edu.cn, x.guo@sjtu.edu.cn

The research on OFET biochemical sensors brings great opportunities for *in situ* biosensor systems. However, current advances are mainly based on proof-of-concept laboratory systems. Both the electrical performance (*e.g.* sensitivity and reliability) and chip integration with scalable processing are key to applications in the on-site detection of analytes. In this regard, the performance of OFET biochemical sensors is governed by the transduction ability of the transistor, the sensing capability of the SE, and their integration reliability. Therefore, device and materials engineering should be considered to promote the design of an OFET biochemical sensor chip as well as to realize device integration for a systematic sensing system.

As a key signal conversion component in sensing systems, the electrical performance of OFET devices has a significant impact on overall sensitivity, power consumption, and stability.[40,41] It has been demonstrated that reducing the subthreshold swing (SS) of an OFET device can not only reduce the operating voltage but also effectively improve the voltage-to-current conversion efficiency, which is useful to develop biosensors.[29] Herein, increasing the unit area capacitance of the gate dielectric and promoting the quality of the organic channels are two primary ways to reduce the SS of the OFET, which can be enhanced by material and device engineering. In addition, materials can also improve the sensing performance of SEs, which contributes to the development of high-performance OFET biochemical sensors. For example, the surface and size effects of nanomaterials enable a larger specific surface area and more efficient catalytic activity, which is attractive for the construction of SEs.[42–44] In electrochemical sensors, nanomaterials can be used as carriers to bind more molecule receptors,[45,46] catalysts for facilitating biochemical reactions,[44,47] conductors to accelerate electron transduction rates,[48] and antifouling materials to stabilize the sensing interface.[49–51] The diversity of nanomaterials can optimize the sensing performance and expand the range of applications for OFET sensors. The integration mode of the SE and OFET determines the form, reliability, and application portability of OFET biochemical sensors. Therefore, addressing integration issues is indispensable to the future of miniaturized multiplexed OFET biochemical sensor chips.

Herein, we summarize the strategies to improve sensitivity and stability from the perspectives of material and device engineering, as well as advanced integration approaches towards practical measurement, which can be a valuable guide to the design of OFET biochemical sensor systems. The review is divided into the following parts: the working principle of OFET-based biochemical sensors in a widely used extended-gate structure is elaborated in Section 2; nanomaterials that have great potential to improve the sensitivity and stability of SEs used in electrochemical sensors are introduced in Section 3; strategies of material and device engineering for building OFET devices with high amplification capacity and stability for biosensors are summarized in Section 4; and the integration approaches and demonstration of OFET-based biochemical sensing systems are presented in Section 5. We omit here the discussion on transistor sensors using the channel as the sensing layer, including electrolyte-gate type and organic electrochemical transistors,[52–56] and the printing techniques and printing processes for electrodes or OFET devices,[55,57–60] which have been well reviewed in earlier work.

2. Operation mechanisms and material requirements of OFET biochemical sensors

2.1 OFETs as a gate voltage-controlled current source

A typical OFET consists of a gate (G) electrode, a gate dielectric layer, an OSC layer, and a pair of electrodes (source and drain electrodes, S/D). Depending on the relative position of the electrodes and the OSC or dielectric layer, OFETs can be divided into four typical structures: bottom gate bottom contact (BGBC), bottom gate top contact (BGTC), top gate bottom contact (TGBC), and top gate top contact (TGTC).[61] Due to the limitations of the manufacturing process and material properties, most solution/printable OFETs are made with BGBC and TGBC structures. The OFET is a kind of voltage-controlled current source device. When an appropriate gate–source voltage (V_{GS}) is applied, a certain number of carriers are induced at the interface of the OSC and gate dielectric. Due to the existence of drain–source voltage (V_{DS}), the accumulated carriers lead to a directional flow of drain current (I_D), the magnitude of which is regulated by V_{GS} (Fig. 1a-I).[53,61] The relationship between I_D and V_{DS} above the subthreshold region can be described by the following equation:

$$I_D = \frac{\mu C_{diel} W}{L}\left(V_{GS} - V_{th} - \frac{V_{DS}}{2}\right)V_{DS} \quad (0 < |V_{DS}| < |V_{GS} - V_{th}|) \tag{1}$$

where μ is the mobility, C_{diel} is the unit area capacitance of the gate dielectric; V_{th} is the threshold voltage; and W and L are the width and length of the channel, respectively. In the subthreshold region, the I_D of an OFET device can be modulated by V_{GS} even by several orders of magnitude (eqn (2)).[62] A linear shift in V_{GS} causes an exponential change in I_D. The I_D is exponential, depending on the V_{GS} and SS of the OFET device (eqn (3)).

$$I_D = \frac{\mu C_{diel} W}{L}\left(\frac{qSS}{\ln(10)k_B T} - 1\right)\left(\frac{k_B T}{q}\right)^2 e^{\frac{\ln(10)(V_{GS} - V_{th})}{SS}}\left(1 - e^{-\frac{qV_{DS}}{k_B T}}\right) \quad (V_{GS} < V_{th}) \tag{2}$$

Thus,

$$I_D \propto e^{\frac{\ln(10)(V_{GS} - V_{th})}{SS}} \tag{3}$$

where q is the elementary charge, k_B is the Boltzmann constant, and T is the absolute temperature.

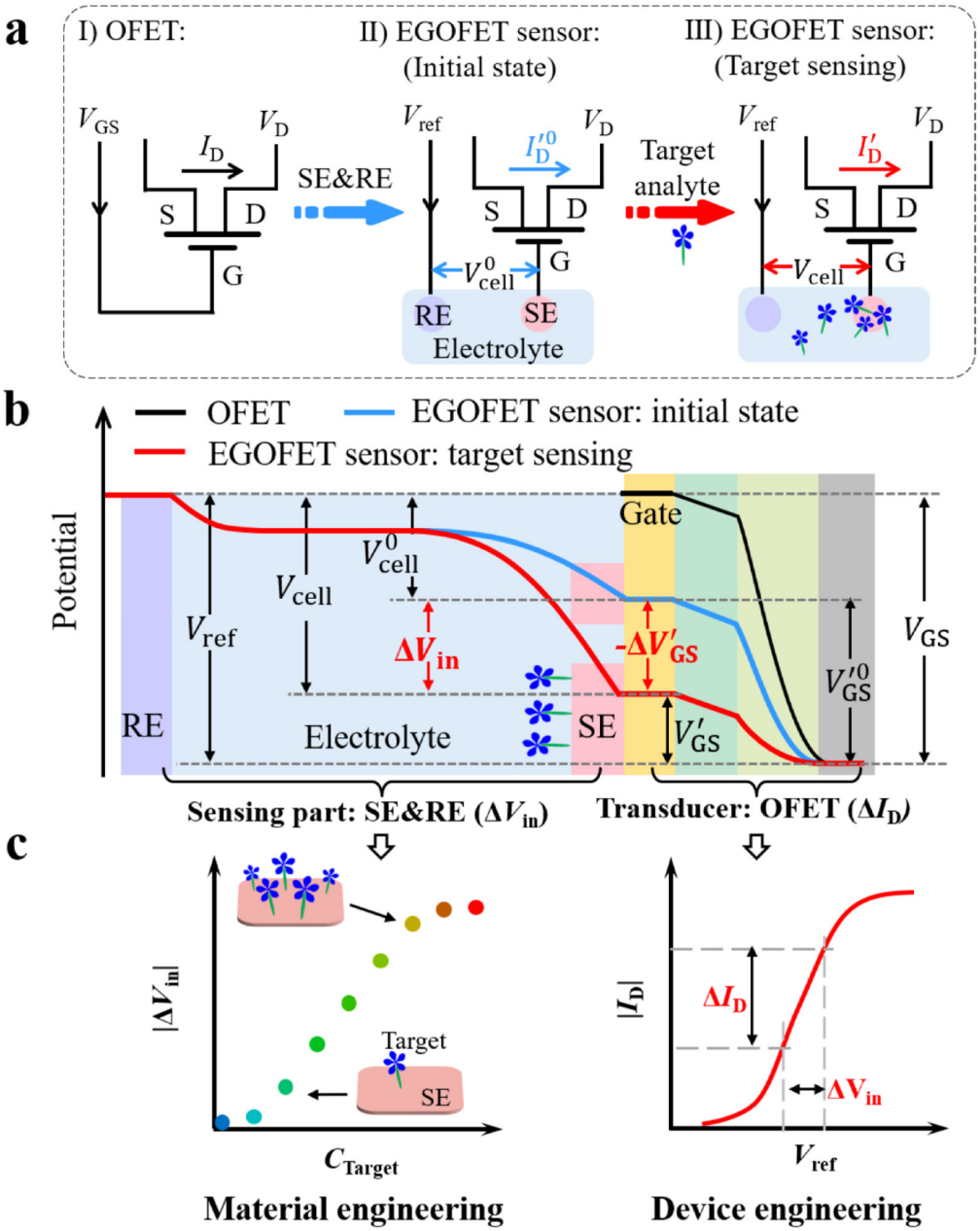

Fig. 1 The structure and sensing mechanism of the OFET biochemical sensor. (a) The simple circuit diagram of (I) OFET device, (II) extended-gate-type OFET (EGOFET) biochemical sensor, and (III) EGOFET sensor with target analytes. For the construction of an EGOFET biochemical sensor, the OFET transducer needs to combine with the sensing part – an electrochemical cell comprising a sensing electrode (SE), a reference electrode (RE), and the test electrolyte. The phase to interface in the electrolytic cell introduces a constant initial potential change (V^0_{cell}) which can cause an initial channel current (I'^0_D). When the measured substance is present, the SE surface develops an interfacial potential (ΔV_{in}) which causes a sensing state of V_{cell} and I'_D. (b) Diagram for the interface potential drop of the EGOFET biochemical sensor with and without analytes. The capture of the target analyte brings a potential shift ΔV_{in} at the SE/solution interface and thus equals $\Delta V'_{GS}$ for the OFET. (c) The two key sensing steps of the OFET biochemical sensor. According to the Nernst equation, the interfacial potential shift ΔV_{in} for the SE is related to the analyte concentration and can be amplified by the introduction of sensitive materials. The output signal I_D is determined by both the input signal ΔV_{in} at the SE interface and the amplification factor (related to SS) of the OFET.

2.2 Working principle of extended-gate OFET biosensors

Since OSCs are susceptible to dissolved oxygen and humidity, it is very challenging to develop OFET biochemical sensors that can operate with high long-term stability and repeatability. EGOFET sensors were thus proposed to isolate the OFET from the wet sensing environment, avoiding damage to the OFET. The schematic diagram and operation mechanism of an EGOFET biochemical sensor are illustrated in Fig. 1. As shown in Fig. 1a-II and III, it has a structure very similar to that of an

OFET but has an additional electrochemical cell consisting of a SE, reference electrode (RE) and electrolyte. The gate of the OFET is connected to the SE and the V_{GS} of the OFET is applied *via* RE–electrolyte–SE and is named the reference voltage (V_{ref}). The potential of the entire electrochemical cell (V_{cell}) is the sum of constant interfacial potentials V^0_{cell} and the concentration-dependent change in interface potential (ΔV_{in}) (eqn (4) and Fig. 1b). Thus, for the EGOFET biochemical sensor, the gate voltage V'_{GS} is controlled by the combination of V_{ref} and V_{cell} (eqn (5)), which finally modulates the channel current I'_D. Thus, the OFET biochemical sensor works by monitoring I'_D changes before and after sensing the biochemical target analytes.

$$V_{cell} = V^0_{cell} + \Delta V_{in} \quad (4)$$

$$V'_{GS} = V_{ref} - V_{cell} \quad (5)$$

The change in the OFET biochemical sensor threshold voltage ($\Delta V'_{th}$) presents the following relationships:

$$\Delta V'_{th} = \Delta V'_{GS} = -\Delta V_{in} \quad (6)$$

This means that variations of the target analyte will lead to changes in ΔV_{in}, and the OFET biochemical sensor will further present changes in $\Delta V'_{th}$ and therefore I'_D. Hence, the operation mechanism of OFET biochemical sensors can be explained by the threshold voltage shift, resulting from either an interfacial potential shift at the sensing interface or charge coupling by the terminal portion.[63,64]

2.3 Key factors affecting the sensitivity performance

An OFET biochemical sensor can be divided into two portions: the sensing part (electrochemical cell) converts the biochemical signal (concentration) into an electrical signal (ΔV_{in}) and the transducer part (OFET) amplifies the small potential changes ΔV_{in} into a current signal (Fig. 1c). The normalized current response ($R = I'_D/I^0_D - 1$) is a function of $\Delta V'_{th}$, which can be derived using eqn (1), (2), and (6), represented as the following expressions:

Above the threshold region:

$$R = \frac{I'_D - I^0_D}{I^0_D} = \frac{V'_{GS} - V^0_{GS}}{V^0_{GS} - V_{th} - \frac{V_{DS}}{2}} = \frac{\Delta V'_{th}}{V^0_{GS} - V_{th} - \frac{V_{DS}}{2}} \quad (7)$$

Near the threshold region:

$$R = \frac{I'_D - I^0_D}{I^0_D} = e^{\frac{\ln(10)}{SS}(V'_{GS} - V^0_{GS})} - 1 = e^{\frac{\ln(10)}{SS}(\Delta V'_{th})} - 1 \quad (8)$$

It is noted that when an OFET transducer operates above the threshold region, R is fair for a certain $\Delta V'_{th}$ caused after target analyte binding on the SE. But R can be remarkably maximized in the subthreshold region. This means that in this region the OFET can convert small gate potential changes into great current changes, which is the basis for developing OFET biochemical sensors for detecting weak signals with high sensitivity.

Here, the initial signal ΔV_{in} is related to the sensing capability of the sensing material on the SE and can be enlarged by employing the sensing material with high affinity with the target analyte, such as nanomaterials. This is true for whatever the OFET operation region is. However, the high current conversion sensitivity R can only be achieved in the subthreshold region, which is also dependent on the SS of OFET devices. Overall, decreasing the SS of the OFET and increasing the ΔV_{in} are two key factors for improving the biochemical sensing performance. In this regard, approaches to improve the sensing performance can be divided into two categories: impoving the inherent interfacial sensitivity of the SE and enhancing the amplification capability of the OFET devices. For these reasons, the materials engineering of sensing interfaces and the device engineering of OFET transducers are urgently desired.

3. Materials engineering for enhancing the sensing efficiency of sensing electrodes

Nanomaterials are integral components in the fabrication of biochemical sensors with high sensitivity and stability. The use of various types of printable nanomaterials, including metallic nanomaterials, carbon nanomaterials, and functional organic nanomaterials, endows the sensing electrodes with superior detection performance through materials engineering. Table 1 presents the widely used printable functional nanomaterials for improving the sensing performance of SEs, which will be detailed in the ensuing discussion.

3.1 Incorporating metallic nanomaterials

Surface effects and small size effects in metallic nanomaterials endow them with a richer set of carrier and active sites and higher electrochemical catalytic activity than those of bulk solid materials.[45,48] Based on their unique properties, noble metal-based nanomaterials are widely used for electrochemical detection and analysis. The introduction of metallic nanomaterials can improve the detection performance by enhancing the conductivity, probe density, and catalytic activity of the electrode surface. To suppress aggregation, metallic nanomaterials are often used in conjunction with supporting materials, such as carbon nanomaterials or organic nanomaterials.[65,66] Due to the synergistic effect, composite materials present higher sensing performance than single materials. A great deal of work has been done to improve the performance of sensing interfaces by using noble metals, metal oxides, and other metal compound nanomaterials. A comprehensive summary is given in the following section.

3.1.1 Noble metal nanomaterials. Noble metal nanomaterials have a large specific surface area, high electrical conductivity, and exceptional catalytic activity, thus improving the detection sensitivity and selectivity of sensor assays.[67–69] Noble metal nanomaterials, such as gold (Au), silver (Ag), and plati-

Table 1 Summary of the functional nanomaterials for improving the sensitivity of sensing electrodes

Sensing materials	Integration method	Target	Application	Sensitivity	Linear ranges	Limit of detection	Ref.
PANI:PSS/PPy:PSS	Inkjet printing	pH	pH	81.2 mV per pH	pH 3–10	NR	89
AuNPs/DNA probe	Self-assembly	Hg^{2+}	Heavy metal ions	12.48 mV dec^{-1}	2.5 pM–2.5 μM	2.0 pM	68
	Screen printing	Cd^{2+}	(environmental pollution)	11.56 mV dec^{-1}		0.62 pM	
		As^{3+}		11.24 mV dec^{-1}		0.17 pM	
PMo_9V_3–Pd@Pt/CNTs/ITO	LBL assembly process	Dopamine	Health monitors	1.02 μA μM^{-1}	2.5×10^{-8}–1.78×10^{-4} M	1.25×10^{-8} M	91
PANI/MWCNTs/CMC	Dip coating	Ascorbic acid	Health monitors	100.63 μA mM^{-1} cm^{-2}	0.05–5 mM	0.01 mM	92
CB/μPAD	Screen-printing	Bisphenol A	Environmental pollution	6.2 μA μM^{-1}	0.1–0.9 μM and 1–50 μM	0.03 μM	93
CB/Na^+ ISM	Drop-casting	Na^+	Artificial sweat	58 mV dec^{-1}	10^{-4}–1 M	63 μM	94
Sericin–CNT	Stencil printing	Hydrogen peroxide	Health monitors	NR	0.6–17 mM	0.6 mM	95
Fe_3O_4/Co_3S_4–SPCE	Drop-casting	As(III)	Heavy metal ion pollution	4.359 μA μg^{-1} L^{-1}	1.0–10.0 μg L^{-1}	0.691 μg L^{-1}	96
ZnO nanoparticles	Ink-jet printing, drop-casting	Picric acid	Environmental pollution	0.2673 μA μM^{-1}	4–60 μM	4.04 μM	97
rGO/anti-CEA	Drip coating	CEA	Tumor biomarker	18.48 kΩ (ng mL^{-1})$^{-1}$	0.1–5.0 ng mL^{-1}	0.05 ng mL^{-1}	98
G/PBSE/ssDNA	Drip coating	DNA	DNA detection platform	24 mV dec^{-1}	25 aM–10 fM	25 aM	99
GA/MOF	Droplet assembly	Cd^{2+}	Heavy metal ions	0.2716 μA V^{-1}	0.01–1.5 μM	9 nM	100
		Pb^{2+}		0.5242 μA V^{-1}	0.001–2 μM	1 nM	
		Cu^{2+}		0.3604 μA V^{-1}	0.01–1.6 μM	8 nM	
		Hg^{2+}		0.3242 μA V^{-1}	0.001–2.2 μM	0.9 nM	
Apt–CNTs–PFcGE	Drip coating	CEA	Tumor biomarkers	0.1282 μA dec^{-1}	1×10^{-15}–1×10^{-8} g mL^{-1}	2.8×10^{-16} g mL^{-1}	101
OMCSi–Zn–Ab	Drip coating	PCT	Human serum	0.236 μA (ng mL^{-1})$^{-1}$	0.05 pg mL^{-1}–80 ng mL^{-1}	0.013 pg mL^{-1}	102

num (Pt), have been widely applied in biochemical sensing, which served as a carrier or catalytic materials for aptamers, antibodies, or enzymes.[42,70,71]

To achieve highly sensitive and stable biochemical sensing, nanomaterials are often used to modify probe molecules to obtain highly stable and dense sensing interfaces. For example, Au nanomaterials are usually used as carrier materials to help modify the DNA probe on screen-printed electrodes (SPEs).[72,73] Abedi *et al.*[72] reported a label-free electrochemical biosensor for studying the interaction of the anti-cancer drug epirubicin (EPI) with the gene of prostate cancer using gold nanocube (Au NC) modified graphite SPEs (Au NPs/GSPEs) (Fig. 2a). The high conductivity of Au NCs accelerated the electron transfer and improved the detection sensitivity. Besides the physical adsorption of DNA strands, Au nanomaterials are widely used as an exceptional carrier for the loading of thiolated probes due to the covalent bonding of the Au–S bond. Del Caño *et al.*[73] constructed a biosensor for SARS-CoV-2 detection using a thiol-functionalized short single stranded DNA (ssDNA) probe. Homogeneous modification of Au NPs by spraying provides stable and abundant bonding sites for the direct immobilization of dithiol-DNA probes, improving the sensitivity and stability of the DNA biosensor (Fig. 2b). To improve the uniformity and stability of Au NPs on the SE, Zhou *et al.*[74] immobilized Au NPs onto the surface of an amine-terminated SE through self-assembly. The functional electrode was used to anchor the thiolated DNA aptamer and then detect interferon-gamma (IFN-γ). The covalent bonding modification of Au NPs on the SE surface and the *in situ* formation of silver nanoclusters (Ag NCs) indicators on the probes made the aptasensor to be highly robust and sensitive.

Besides, the excellent conductivity and catalytic ability of noble metal nanomaterials also make them ideal sensing materials with high sensitivity.[48,71] And compared with single nanomaterials, complex nanomaterials often present high sensing performance.[5] For example, bimetallic platinum–palladium nanoparticles (PtPd NPs) have high electrocatalytic activity and can be used to directly detect H_2O_2 or H_2O_2-related reactions. Wu *et al.*[65] reported a dual-mode aptasensor for microcystin-LR (MC-LR) based on the MoS_2–PtPd NP modified electrode. MoS_2–PtPd acts as a substrate to obtain a higher aptamer loading, and the signal was amplified by the catalytic activity of H_2O_2. The linear range and detection limit of such methods were 0.1–50 ng ml^{-1} and 0.045 ng ml^{-1}, respectively. Besides, Li *et al.* established a signal-off biosensor for detecting adenosine triphosphate (ATP), which was based on porous composite materials of Fe_3O_4@covalent organic framework-immobilized Au NPs (Fe_3O_4@COF–Au NPs).[75] Due to the cooperative effect between Au NPs and Fe_3O_4, Fe_3O_4@COF–Au NPs presented higher catalytic activity than single-component Au NPs, realizing the ultrasensitive detection of ATP with a detection limit of 16 pM.

3.1.2 Metal oxide nanomaterials and other metal nanomaterials. Due to the excellent biocompatibility and adsorption, metal oxide nanomaterials can effectively immobilize biomolecules and be used to prepare immunosensors, enzyme sensors, and DNA sensors.[45] In addition, they can be used as

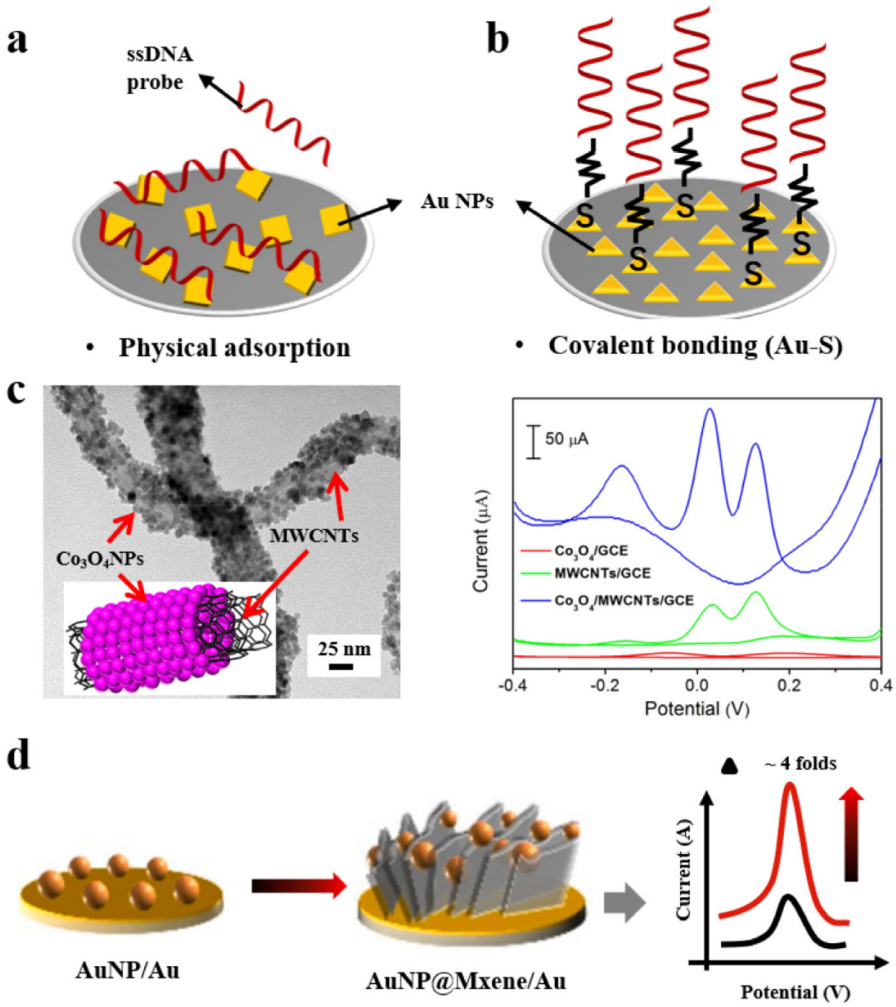

Fig. 2 Metallic nanomaterials incorporated at the electrochemical sensing interface provide stable probe immobilization and signal amplification. (a) Gold nanocube-modified graphite screen-printed electrodes (AuNCs/GSPEs) were used as substrate electrodes for the immobilization of the ssDNA probe *via* physical adsorption between Au and DNA. Reprinted with permission from ref. 72. Copyright 2021, Elsevier. (b) Immobilization of the SH-ssDNA probe by a strong chemical bond between Au and S helps to enhance the robustness of the DNA probe modification and further improves the stability of the sensing. Reprinted with permission from ref. 73. Copyright 2022, Elsevier. (c) TEM image of the Co_3O_4/MWCNT nanocomplex, where the catalytic stability of the Co_3O_4 NPs under alkaline conditions and the high electrical conductivity and excellent adsorption of the MWCNTs contribute to the highly sensitive detection of dihydroxybenzene in the ocean. Reprinted with permission from ref. 66. Copyright 2019, Elsevier. (d) Schematic diagram of using Au NP@Mxene modified Au screen-printed electrodes (SPEs) which provided a higher electrochemical signal than Au NPs modified Au-SPEs. Reprinted with permission from ref. 78. Copyright 2020, Elsevier.

catalysts or enzyme-like materials due to their intrinsic redox chemistry, variable oxidation states, and tunable physicochemical and morphological properties. Compared with single metal oxide nanomaterials, composite nanomaterials present higher sensing performance.[76] The composition with different metals will also produce an excellent synergy effect, thereby improving their performance, stability, and anti-interference ability at the sensing interface, showing good application prospects.

The enzyme-like catalytic activity of transition metals, such as CuO, Co_3O_4, NiO, and $NiCo_2O_4$, can be used for enzyme-free sensing, eliminating the sensitivity of enzyme sensors to the environment, and improving the robustness of the sensors. The crystal structure and morphology can influence their catalytic activity. Song *et al.* prepared an urchin-like bimetal oxide $NiCo_2O_4$, showing higher oxidase-like activity than that of the flower-like one.[47] What's more, the composition with the supporting material can effectively inhibit the aggregation of small nanoparticles and improve their electrical properties. Zhao's group established an electrochemical sensor for the simultaneous determination of catechol (CC) and hydroquinone (HQ) by Co_3O_4/MWCNTs.[66] Co_3O_4 uniformly distributed on MWCNTs had a higher surface area and fast electron transfer efficiency than the agglomerated one (Fig. 2c). Composite nanomaterials combined the high catalytic activity of Co_3O_4 under alkaline conditions with the excellent electrical conductivity of MWCNTs, which can be applied to the detection of dihydroxybenzene contamination in the marine

environment. Dayakar *et al.* reported a non-enzyme glucose sensor based on CeO_2@CuO core–shell nanostructure modified SPEs.[77] The catalytic activity of CeO_2@CuO core–shell nanocomposites was enhanced by a synergetic effect, which can be attributed to the oxide ion vacancies generated. By the combination of the high catalytic activity of CuO nanomaterials and the outstanding electron transfer rate of CeO_2, enzyme-free glucose sensors present an excellent specific sensitivity of 3319.83 μA mM^{-1} cm^{-2}.

In addition to metal oxides, metal sulfides, metal nitrides, metal carbides and metal–organic frameworks (MOFs) also have a very important influence in the field of electrochemical sensing.[79] These materials are usually used to facilitate the immobilization of the recognition probe to amplify the response signals. Martínez-Periñán *et al.*[80] used MoS_2 as a carrier substrate material for bonding of a thiolated ssDNA probe, which was further applied to detect InIA gen in *Listeria monocytogenes* bacteria and the ORF1ab sequence of SARS-CoV-2. Likewise, Mohammadniaei *et al.* proposed a sensitive oncomiR biosensor based on Au NPs/MXenes.[78] It was found that the synergistic effect of Au NPs and MXenes significantly increased the sensitivity of the biosensor, where the signal was amplified by a factor of nearly four (Fig. 2d). Kong's group constructed a label-free microRNA biosensor based on GOx encapsulated zeolitic imidazolate framework-8 (ZIF-8).[43] The encapsulation of enzymes by ZIF-8 could preserve their biological activity even in harsh environments. The cascade catalysis reaction could be triggered in the confined space of ZIF-8 nanoreactors, and the 3D DNA walker was used for signal amplification. The proposed miRNA-21 sensor has a wide dynamic range from 0.1 nM to 10 μM with a low detection limit of 29 pM, which shows great potential in the early diagnosis of cancers.

3.2 Employing organic nanomaterials

Due to their abundant functional groups, organic materials usually have the functions of recognition and anti-pollution, which are indispensable in the construction of biosensing electrodes. Aptamers and molecularly imprinted polymers (MIPs) are ideal synthetic bioreceptors due to their controllable fabrication process, and high affinity with the target protein. They present outstanding robustness in a wide pH range or high temperature, superior to natural antibodies. Besides, conductive polymers are considered to be very promising sensing materials due to their electrical behavior and tunable sensing capability functions. By chemically grafting functional groups or combining them with other nanomaterials, the conductive polymer can be applied in bioelectrochemical sensing with outstanding performance. The following will briefly introduce aptamers (DNA, peptides), MIPs, and conductive polymers (PANI, PPy, PEDOT:PSS) applied in biochemical sensors.

3.2.1 Aptamers. Similar to antibodies, aptamers have affinity and specificity with the target substance.[81] The dissociation constant (K_D) value of a DNA aptamer with the target was of the order of nM–pM.[82] In addition, aptamers have many advantages over antibodies, such as lower production costs, ease of chemical modification, smaller size, and lower immunogenicity, which are considered to be the best alternative to antibodies in the future.

Curti *et al.* constructed an aptasensor for SARS-CoV-2 spike protein, based on redox-tagged DNA aptamer modified single-walled carbon nanotube SPEs (SWCNT-SPEs).[83] The dissociation constant (K_D) value of the DNA aptamer with the target spike protein was 43 ± 4 nM, which is equal to the K_D of antibody–antigen. The high K_D contributed to the high selectivity and sensitivity of the aptasensor, resulting in a detection limit of 7 nM. Because the labeling of aptamers may lead to additional processes and costs, the label-free sensor has greater potential for future analysis. Kwon *et al.*[84] proposed a label-free aptasensor based on the surface potential change induced by the specific binding of the target protein (Fig. 3a). The FET-based sensor was modified with the DNA aptamer for the detection of the hemagglutinin (HA) protein of the highly pathogenic H5N1 avian influenza virus (AIV). The capture of the HA protein could cause a conformational change of the aptamer, which could further affect the surface potential of the electrode due to the electrification of the aptamer. The aptamer sensor was successfully applied to the detection of the HA protein in chicken serum, and the detection limit was 5.9 pM. Chen *et al.*[50] proposed an ultralow fouling cancer biomarker sensor by combining antifouling peptides with recognized DNA probes. Electrochemical biosensors show excellent anti-fouling ability and excellent sensing performance in complex human body fluids including serum, sweat, and urine.

3.2.2 Molecularly imprinted polymers (MIPs). Molecularly imprinted polymers (MIPs) contain sites that are complementary in the morphology of the functional groups of the template molecule. Compared to antibodies, MIPs are not only specific to the target analyte but also more stable and reproducible. McClements *et al.*[85] constructed a highly robust nano-MIP sensor for the rapid (15 min) clinical detection of SARS-CoV-2. Nano-MIPs were rapidly synthesized in 2 h using tiny SARS-CoV-2 antigen fragments. The K_D value of nano-MIPs and the target spike protein was 7 nM, which is higher than the affinity of antibodies. Even after autoclaving at 121 °C for 85 min, K_D remained at 3 nM, demonstrating that nano-MIPs had more stable affinity than antibodies. Nano-MIPs with high affinity could be easily modified on SPEs by electrografting and coupling reactions and applied to detect alpha and delta variants of spike protein, with detection limits of 9.9 fg mL^{-1} and 6.1 fg mL^{-1}, respectively.

Besides the affinity with antigens, MIPs can be applied for the detection of small molecules. Minami and colleagues developed a tropane alkaloid sensor using modified MIPs on the extended gate of the OFET device (Fig. 3b).[86] MIPs were synthesized by free radical polymerization and optimized by different molar ratios. The *in situ* synthesized MIP SE showed excellent selective discrimination for (*S*)-hyoscyamine. Following the capture of (*S*)-hyoscyamine, the surface potential would change, resulting in a V_{th} shift of the OFET biochemical

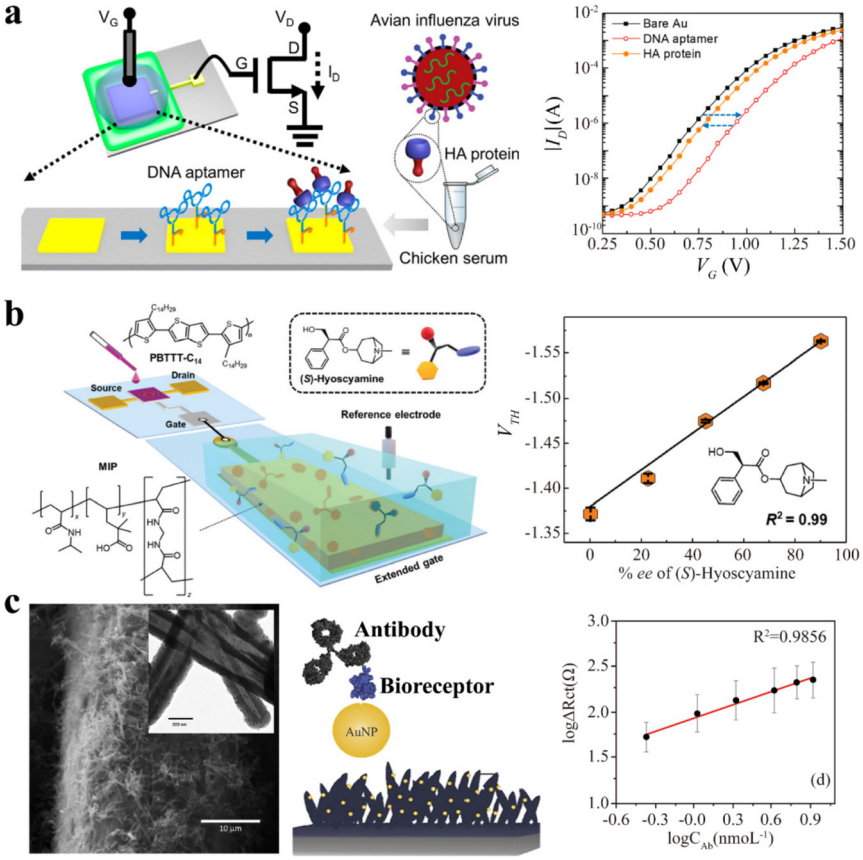

Fig. 3 Organic nanomaterials incorporating electrochemical SEs enhanced the diversity and robustness of the sensing interface. (a) Schematic diagram of the aptamer modified extended-gate FET for AIV detection. After the negatively charged DNA aptamer was immobilized, the V_{th} value of the FET shifted positively, but after binding with the HA target, it shifted negatively due to the conformational change of the DNA aptamer. Reprinted with permission from ref. 84. Copyright 2020, American Chemical Society. (b) Schematic representation of an OFET biochemical sensor with a molecularly imprinted polymer (MIP) modified extended Au gate for accurately quantifying tropane alkaloids. The MIPs showed a greater response to tropane alkaloids. Reprinted with permission from ref. 86. Copyright 2022, the Royal Society of Chemistry. (c) Schematic representation of PPy–AuNP modified electrodes for the detection of SARS-CoV-2 nucleocapsid protein monoclonal antibodies. Reprinted with permission from ref. 90. Copyright 2022, Elsevier.

sensor. They also reported a taurine OFET biosensor using synthetic MIPs.[37] The detection limit was only 0.33 μM, which was even lower than the test result of the high-performance liquid chromatography (HPLC) method. The use of MIPs in biochemical sensors expands the opportunities for the detection of a wide range of molecules.

3.2.3 Conductive polymer materials. Conductive polymers are an important class of functional materials that have been widely used in the preparation of electrochemical biosensors due to their tunable chemical, electrical and structural properties. They can be designed by chemically grafting functional groups, and nanostructures, or combined with other functional materials such as Au nanoparticles. The application of conductive polymer materials, such as poly(3,4-ethlenedioxthiophene) (PEDOT:PSS), polyaniline (PANI) and polypyrrole (PPy), for biosensors can greatly improve the sensitivity, selectivity, stability, and reproducibility.

Gao *et al.* reported a wearable sensor array for multiplexed *in situ* sweat analysis in which PEDOT:PSS was employed as the ion-to-electron transducer layer for sodium and potassium ions (Na^+, K^+).[87] Due to the high redox capacitance of PEDOT:PSS, ion-selective electrodes (ISEs) of Na^+ and K^+ show excellent sensitivity close to the Nernstian theoretical limit. PANI can not only be used as a solid contact material but also be used as a pH sensitive material, because of its proton doping and deprotonation in different oxidation states. Gosselin *et al.* reported a sensor for the real-time monitoring of the DNA amplification process based on a screen printed PANI sensing electrode.[88] The developed pH sensor had a super-Nernstian sensitivity of 82.86 mV per pH and can even be used to detect loop-mediated isothermal amplification (LAMP) of DNA strands with only 10 copies. Zea *et al.* also fabricated a flexible pH microsensor based on a mixed conductive polymer of PANI and PPy using inkjet printing (IJP) technology.[89] In a wide pH range (pH 3–10), the fully printed pH electrode showed a high sensitivity (81.2 mV per pH) and excellent reproducibility. Hryniewicz *et al.* reported an impedimetric immunosensor for SARS-CoV-2 nucleocapsid protein monoclonal antibody detec-

tion by PPy–AuNP modified electrodes.[90] The higher specific area of PPy nanotubes allowed them to exhibit higher sensitivity than that of the globular morphology and a low limit of detection of 0.386 ng mL^{-1} (Fig. 3c).

In addition, organic small molecules are also indispensable in the construction of biochemical sensing electrodes. They can be used as interface engineering materials to assist in binding bioreceptors to improve stability, or as blocker molecules to hinder nonspecific adsorption and improve the selectivity of biosensors.

3.3 Using carbon nanomaterials

The family of carbon materials includes many members, due to the sp^1, sp^2, and sp^3 hybridization of carbon atoms. Important allotropes ranging from zero-dimensional carbon quantum dots and fullerenes to one-dimensional carbon nanotubes (CNTs), two-dimensional graphene, three-dimensional ordered mesoporous carbon (OMC), and graphite have demonstrated a great improvement in the sensitivity and reliability of sensing electrodes (Fig. 4a).

Although carbon materials with different dimensions show great differences in the morphology and structure, their physical and chemical properties behave similarly:

(a) Excellent electrical conductivity: the conductivity value of pure graphene reaches 10^8 S m^{-1}, and that of pure CNTs is more than 10^6 S m^{-1},[103] even for graphite, the conductivity parallel to the crystal plane reaches 10^4 S m^{-1}.[104]

(b) Extremely high specific surface area: the theoretical specific surface area of pure graphene is 2630 m^2 g^{-1},[105] and that of single-walled CNTs is 1315 m^2 g^{-1}.[106] As for OMC, the specific surface area reported in the literature can be up to 2500 m^2 g^{-1}.[107]

(c) High chemical modifiability: the presence of a large number of defective sites on the surface of carbon materials allows them to be easily modified by functional groups.

(d) Solution treatment process: graphene can be prepared by liquid-phase exfoliation of graphite,[108] and OMC sheets can be prepared by hydrothermal treatment and carbonization.[109] Those powdered carbon materials also can be uniformly dispersed in a suitable solvent, which guarantees the uniformity of post-treatment.

Therefore, the application of carbon materials in SE can greatly improve the detection ability of target molecules. Furthermore, the enhanced sensitivity can be translated into better sensor performance by OFETs. The following is a review of typical cases of biosensors in which carbon materials play an irreplaceable role in the construction of electrode functions.

3.3.1 Graphene. Graphene has a single-layer structure composed of sp^2 hybrid carbon (π-electron structure) with a theoretical thickness of about 0.3 nm, which results in a very large specific surface area and an ultrahigh theoretical charge carrier speed (~10^6 m s^{-1}). Recently, graphene surface modification of functional groups, enzymes, antibodies, or aptamers

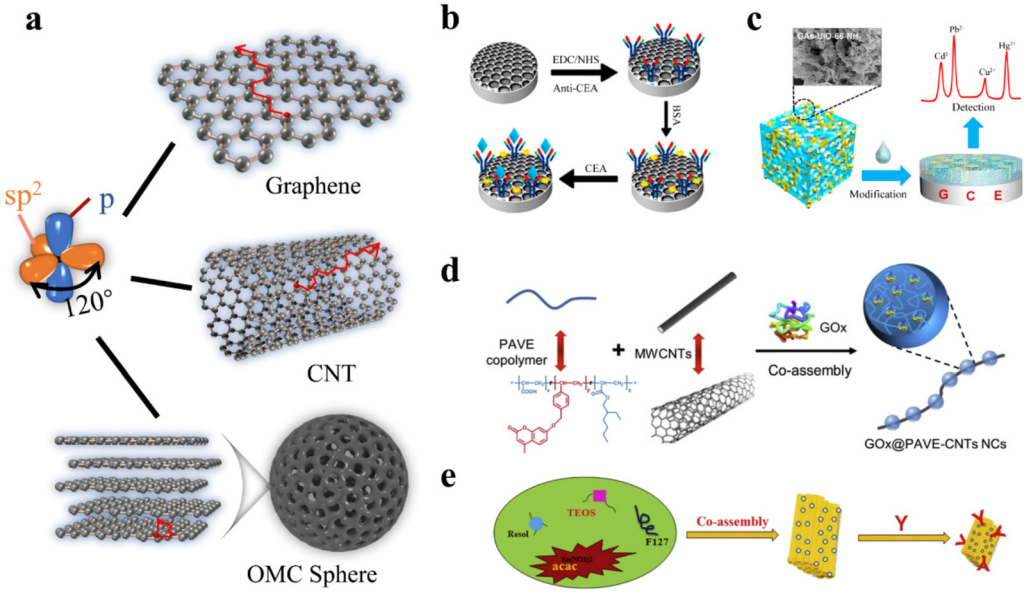

Fig. 4 Carbon nanomaterials incorporated in the electrochemical sensing interface. (a) The sp^2 hybridization of carbon and the diagrams of graphene, CNTs, and an OMC sphere, the inset of the OMC sphere indicate the graphitized structure on its surface. (b) Schematic diagram of using NHS/EDC as an intermediate molecule to link graphite and antibody. Reprinted with permission from ref. 98. Copyright 2021, Elsevier. (c) Schematic diagram of the three-dimensional GA–MOF composite for constructing heavy metal ion sensitive electrodes, the top-left inset shows the SEM of GA–MOFs. Reprinted with permission from ref. 100. Copyright 2019, American Chemical Society. (d) Schematic illustration of the preparation of the GOx-loading hybrid nanocomposite PAVE–CNTs *via* one-step co-assembly. Reprinted with permission from ref. 101. Copyright 2021, Elsevier. (e) Schematic illustration of the loading of Zn NPs and PCT primary antibody on the OMCSi surface for pre-enrichment of PCT in solution. Reprinted with permission from ref. 102. Copyright 2018, Elsevier.

for the enhancement of sensitivity and selectivity in target molecule detection has been widely studied.

Pristine graphene needs to be modified to adapt the biochemical sensing electrodes because of lacking active sites to react with other substances. Typically, graphene oxide (GO) introduces abundant functional groups including hydroxyl, carbonyl, carboxyl, and epoxy groups. Jozghorbani *et al.*[98] used an EDC/NHS linker to activate the carboxyl group on the reduced GO, followed by the attachment of antibodies to construct electrodes sensitive to carcinoembryonic antigens (CEAs) (Fig. 4b). The proposed immunosensor exhibited a low LOD (0.05 ng mL^{-1}) and high sensitivity (0.1–5 ng mL^{-1}), benefiting from the abundant anchoring sites on reduced GO.

Owing to the unique π-electron structure, π–π stacking and electrostatic interactions are viable approaches to anchor functional molecules to graphene. Most of the intermediates have a benzene ring structure that can non-covalently attach to the graphene, and a functional group that can covalently attach to biomolecules, such as 1-pyrenebutyric acid succinimidyl ester (PBSE) containing a pyrene group[99] and a thionine (THI) containing benzene ring.[110] Campos *et al.*[99] developed a graphene electrolyte-gated FET sensor for the label-free detection of DNA hybridization, using PBSE to anchor the probe ssDNA. The high specific surface area of graphene supported sufficient probe loading and enhanced the transduction capacity of the graphene–electrolyte interface, which increased the sensitivity of the sensor.

The recently developed three-dimensional graphene network can also be used to immobilize functional components by providing domain-limited space. Lu *et al.*[100] prepared graphene aerogels–metal–organic framework (GA–MOF) composites *via in situ* growth of MOF crystals on GA (Fig. 4c). Due to the interaction between the hydrophilic group of MOFs and heavy metal cations, the GA–MOF based sensor achieved selective detection of multiple heavy metal ions. The graphene served as a support matrix for MOFs and also compensated for the poor electrical conductivity of MOFs by accelerating electron transfer.

3.3.2 Carbon nanotubes (CNTs). CNTs can be viewed as graphene sheets curled into columns. Apparently, the electron cloud distribution of the convoluted graphene sheets (CNTs) changes dramatically from a symmetric distribution on both sides to an asymmetric distribution on the inside and outside of the cylinder, which leads to CNTs with higher electrochemical activity along the tube than graphene. Coupled with the long length of CNTs (more than 100 μm), CNTs can serve as an excellent electron transport intermediate in electrochemical sensing. These unique properties of CNTs suggest a wide range of potential application scenarios in biosensors.

Appropriate functionalization and immobilization are critical to allow the preparation of biosensing electrodes utilizing CNTs. Breslin *et al.* introduced carboxyl groups on the MWCNT surface and then grew Au nanoparticles (NPs, 7.5 nm) *in situ*.[111] The Cr(VI) ion-sensitive electrode (ISE) was prepared based on this composite, and has a low LOD of 7.2×10^{-7} M. Carboxyl-functionalized CNTs enhanced their dispersion in solution, accompanied by the attraction to the Au core at the position of the functional group. The performance of this composite was naturally enhanced since Au NPs acted as catalytic sites for the reduction of Cr(VI).

CNTs often require auxiliary materials in the loading of macromolecules due to the large size difference.[112,113] A common strategy is to use a polymer–CNT composite as a loading matrix. Xu *et al.* constructed a glucose biosensor[113] based on the GOx@PAVE–MWCNT bio-nanocomposite which displayed a low LOD (0.36 μM) and a wide linear range (1.0 μM–5 mM) (Fig. 4d). The PAVE maintained the bioactivity of GOx and prevented the GOx from leaching out of the electrode, while the CNTs tandem with these GOx–PAVE nanoparticles were equivalent to "electron tunneling", allowing the collection of electrons generated by the enzymatic electrochemical reaction and transmit them to the conducting substrate.

Besides direct drop coating on the electrode surface, functionalized CNTs can also act as signal amplifiers for target molecules, benefiting from the good conductivity of CNTs and abundant electroactive sites of modifiers. A novel electrochemical aptasensor assembling the CEA-aptamer and poly (ferrocenyl glycidyl ether)-grafted CNTs (PFcGE–CNTs) was reported by Li *et al.*[101] After capturing the CEA by the aptamer, the electrochemical signal was significantly amplified for the excellent electrochemical activity of the ferrocene derivatives contained in PFcGE–CNT composites.

3.3.3 Ordered mesoporous carbon (OMC). The high specific surface area of OMC is derived from a well-defined ordered pore structure of 2–50 nm, a size that is well-matched to most catalysts. OMC materials are prepared by calcination of organic precursors, thus atomic doping and functional group modification can be easily achieved, which provides more advantages in catalyst loading.

The intrinsic properties of the original OMC material can enhance ion–electron trans-conductivity in ion selective electrodes (ISEs), where the ordered pore channels facilitate the mobility of ion carriers, the high specific surface area increases interfacial capacitance, and the good electrical conductivity realizes the rapid transfer of electrons. Liu's group developed a K^+ ISE using OMC spheres as a transduction layer that resulted in high sensitivity (63.5 ± 0.6 mV dec^{-1}) and a wide linear range ($10^{-4.19}$–$10^{-0.21}$ M).[49] The stability of K^+ ISE also was increased because the hydrophobicity of the OMC avoids the water layer.

In the current study, the heteroatoms doped during the preparation to enhance the electrocatalytic ability of OMC is a common modification strategy. Zhang *et al.* proposed an L-tryptophan (Trp) sensor based on an N-doping OMC/Nafion electrode, which showed a low LOD (35 nM) with a high sensitivity (6.14 A M^{-1} cm^{-2}).[114] N-doping not only increased the active sites and surface charge density of OMC, but also improved the electron transfer rate of the carbon matrix.

When loading catalysts such as biomolecules and metal nanoparticles, it is necessary to modulate the mesoporous structure of OMC to avoid catalyst aggregation and modify the

surface of OMC to ensure stable catalyst loading. Fang's group synthesized Zn NPs on the OMC surface, followed by coupling with the procalcitonin (PCT) primary antibody to fabricate PCT electrochemical sensors (Fig. 4e).[102] The Zn NPs and PCT primary antibody were heavily loaded on the surface, which in turn allowed the signal of protein electrochemical detection to be amplified as much as possible.

4. Device engineering for improving the OFET transduction performance

Integrating OFETs into electrochemical sensors can amplify the signal and ameliorate the requirement for a readout system. As discussed earlier (Section 2.3), the most important task of device engineering is to enlarge the OFET amplification ability with a steep SS. Moreover, the reduction of SS is also helpful for lowering the operation voltage and therefore the power consumption. Li *et al.*[115] proposed diverse OFETs of different SSs by constructing different device structures with different insulating materials, verifying the relationship between the SS and the maximum conversion efficiency of OFETs experimentally. By comparing the developed OFETs with a commercial Si-FET in a pH-sensing system, it was demonstrated that reducing the SS of OFETs can effectively improve the sensitivity of the sensing system. Though the resulting sensitivity was similar due to the same level of SS, the power consumption of the OFET sensor was two orders of magnitude lower than that of the Si-FET.

At the same time, the stability of the OFET is another key figure of merits for constructing high-performance integrated biosensors. During the last few decades, plenty of work has been done for reducing the SS to improve the amplification factor and also enhance the stability of printable OFETs using a combination of material and device engineering.

4.1 Strategies for reducing the subthreshold swing (SS)

In theory, the SS of an OFET is related to the capacitance of the C_{diel} and effective sub-gap density of states (N_{SS}), as shown below (eqn (9)):

$$SS = \ln 10 \cdot \frac{k_B T}{q} \cdot \left(1 + \frac{q^2 N_{SS}}{C_{diel}}\right) \quad (9)$$

where k_B is the Boltzmann constant, T is the absolute temperature, and q is the elementary charge. Therefore, increasing the C_{diel} and decreasing N_{SS} are two primary methods for decreasing SS, which, however, is challenging when OFETs were fabricated on flexible substrates by a low-temperature printable process over a large area.

4.1.1 Enlarging the unit area gate dielectric capacitance (C_{diel}). There are two primary methods for increasing the C_{diel} to decrease the SS of the device: (1) decreasing the thickness of the dielectric layer or (2) introducing high-k dielectric materials. However, decreasing the thickness of the dielectric layer is at the risk of the poor yield of the device due to large dielectric leakage current and the latter is the preferable method. Conventionally, high-k organic materials and ion-gel materials have been widely adopted to boost the development of low-voltage OFETs with steep SS.

4.1.1.1 Organic high-k dielectric materials. Poly(vinyl alcohol) (PVA), poly(4-vinylphenol) (PVP) and P(VDF–TrFE–CFE) are commonly utilized high-k polymer materials for achieving ultra-small SS values of the devices. Conti *et al.*[9] adopted PVP as a dielectric material with a permittivity of around 7.0 and fabricated a device with BGBC architecture through ink-jet printing. The C_{diel} was increased up to 15 nF cm^{-2} and the SS was decreased to 300 mV dec^{-1}. Although PVA has high permittivity for small SS and low voltage operation, the existence of a hydroxyl group may bring challenges to operational stability. To screen the detrimental effects of PVA without sacrificing the total capacitance of the dielectric layer, a self-assembled monolayer (SAM) of *n*-octadecyltrichlorosilane (OTS) was introduced in the work of Liu *et al.* to form an interface layer between the channel and the gate dielectric.[116] As a result, the capacitance of the OFET device based on the PVA/OTS dielectric system was increased up to 28 nF cm^{-2}. In this method, the device met the requirement for low voltage operation (~3 V) and showed a small SS of around 330 mV dec^{-1}. Recently, a kind of relaxor ferroelectric material (P(VDF–TrFE–CFE)) with a high-k value (>60), which can be deposited by a solution process, was introduced to the development of OFET devices. As a pioneering work, Li *et al.* exploited the spin coating process for preparing the P(VDF–TrFE–CFE) layer with the capacitance reaching 330 nF cm^{-2} to develop low-voltage polymer OFETs (Fig. 5a). The resulting OFETs with TGBC

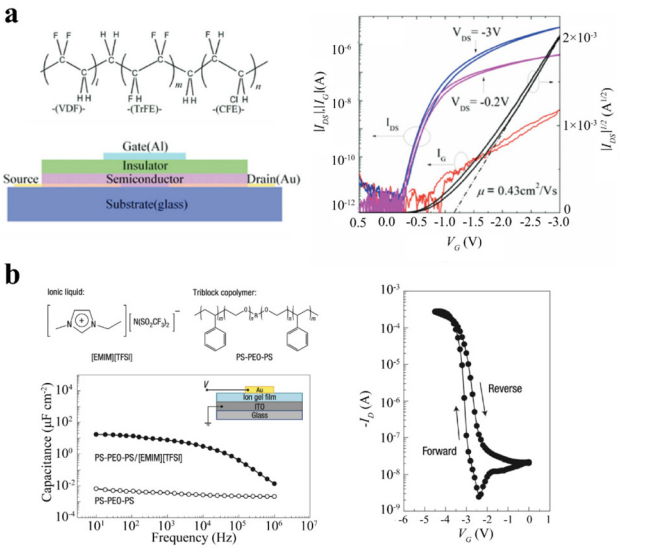

Fig. 5 Decreasing SS by enlarging the unit area gate dielectric capacitance (C_{diel}). (a) Introduction of a high-k dielectric layer of P(VDF–TrFE–CFE) (k > 60) for fulfilling low voltage operation and ultra-small SS. Reprinted with permission from ref. 3. Copyright 2012, Wiley-VCH. (b) Adoption of ion gels for forming an electrical double layer (EDL) of an ultra-high capacitance of up to 10 μF cm^{-2}. Reprinted with permission from ref. 10. Copyright 2008, Springer Nature.

architecture showed extremely low SS of around 97 mV dec^{-1} with less hysteresis.[3] Although increasing the C_{diel} by adopting a high-*k* material is beneficial for decreasing the SS, the polarization of the high-*k* material will bring the challenges of poor stability at a long-term bias and the methodologies for inhibiting dielectric polarization will be summarized in the next part.

4.1.1.2 Ion-gel dielectric materials. Ion-gels can be used as dielectric layers with extremely high capacitance for an ultra-small SS and low voltage operation due to the formation of an electrical double layer (EDL) at the interface. Cho *et al.* utilized [EMIM][TFSI] and PS–PEO–PS as the dielectric layer and increased the gate capacitance up to 11 μF cm^{-2}. In this way, the SS of the device was decreased to 100 mV dec^{-1} (Fig. 5b).[10] Lee *et al.* changed the ionic liquid from [EMIM][TFSI] to [BMIM][PF_6] and the capacitance was increased up to 37 μF cm^{-2} at a frequency of 10 Hz. Devices showed a small threshold voltage of −1.3 V and an ultra-low SS of 110 mV dec^{-1}.[117] It is noted that ion-gels are beneficial for achieving an extremely high C_{diel}, but the frequency response is poorer than those of traditional dielectric materials. This may be a great concern for application to high-speed OFET circuits, but not for the biochemical sensor as the frequency is always low. However, the migration of ions into an organic semiconducting film will bring stability issues, leading to challenges in the biochemical sensing performance of OFETs.

4.1.2 Reducing the sub-gap density of states (N_{SS}) in the channel

4.1.2.1 Phase separation of the semiconductor/polymer blend. Blending small molecules with polymers is an efficient method for increasing the crystal quality and decreasing the N_{SS} by spontaneous phase separation. Small molecules exhibit the merit of higher mobility but face processing challenges in poor film uniformity due to their fast crystallization and strong anisotropic properties. Conversely, high viscosity and amorphous properties make polymers advantageous in film uniformity with the sacrifice of high mobility. Therefore, strategies of blending small molecules with polymers have been proposed to combine the intrinsic merits of each material for achieving higher mobility, better uniformity, and solution processibility. In such a multi-component system, a spontaneous phase separation process may be triggered during the solidification process. Moreover, evaporation-induced concentration gradient and crystallization-induced driving force are found to be two main factors for facilitating phase separation. For the former, when the solvent evaporates from the surface, more soluble components will aggregate to the top surface, resulting in two different phases. For the latter, molecules with strong crystallization properties tend to migrate to the nucleus for crystal growth while the other components with poor crystallization properties will be expelled to the other side, contributing to the final phase separation.[118]

Phase separation of this kind of blending material system has been proven to increase the mobility of OFETs due to the increased π-orbital overlap and electronic delocalization degree of the organic semiconductor film in addition to the improvement of solution processibility and uniformity.[119,120] In addition, a lower trap concentration also ascribing from phase separation was also observed and used to significantly reduce the SS.[12,121,122] Feng *et al.* blended polystyrene with 6,13-bis(triisopropylsilylethynyl)-pentacene and spin-coated them onto a dielectric layer.[123] Ordered, ultra-thin (~10 nm) small molecule stacking with an ultra-low N_{SS} tended to form in the channel layer. The resulting OFETs even with a small C_{diel} (12.2 nF cm^{-2}) achieved a small SS of 100 mV dec^{-1}. Based on this semiconductor material system, Tang *et al.* adopted an ultra-thick SU8 layer (1.16 μm) as a dielectric layer and demonstrated low voltage operation (~5 V) with a small SS of 250 mV dec^{-1} at an ultra-small C_{diel} (~3 nF cm^{-2}). The extracted effective N_{SS} was around 5.79 × 10^{10} eV^{-1} cm^{-2}, which was ascribed to the phase separation.[124]

In addition to the 6,13-bis(triisopropylsilylethynyl)-pentacene/polystyrene material system, phase separation of a high quality channel layer has also been successfully demonstrated in other material systems such as 7-dioctyl[1]benzothieno[3,2-*b*][1]benzothiophene (C_8-BTBT)/polystyrene and 2-decyl-7-phenyl-[1]benzothieno[3,2-*b*][1]benzothiophene (Ph-BTBT-10)/polystyrene.[4,125] Jiang reported the blending of C_8-BTBT with polystyrene to fabricate an ink-jet printed OFET, which demonstrated an extremely low SS (60.2 mV dec^{-1}), approaching the theoretical limit (59.6 mV dec^{-1}).

4.1.2.2 Deposition of high-quality crystals. In addition to the material optimization by a small molecule and polymer blend, process optimization for forming high-quality small molecule stacking is another method for achieving a low N_{SS}. Kunii *et al.* deposited a liquid crystal material (Ph-BTBT-10) to form a high-quality channel of low trap density on polystyrene buffer and achieved an average SS of 102 mV dec^{-1} among 20 different devices.[4] Similar to this work, Kitahara *et al.* developed a novel method for constructing a high-quality single crystal film onto a hydrophobic surface with BGBC device architecture (Fig. 6a). The pre-prepared U-shaped metal film onto the CYTOP film extended the meniscus line and enabled successive film growth. In this way, a highly ordered single crystal of the Ph–BTNT–C_n film was obtained onto the CYTOP film, presenting a low N_{SS} and SS down to 0.91 × 10^{10} eV^{-1} cm^{-2} and 63 mV dec^{-1}, respectively.[5] In the work of Huang *et al.*, a high-quality channel made from blended materials was delivered using a proposed advanced coating process-soft contact coating (SCC) (Fig. 6b). The rotatable blade design made stress applied to the substrate to be minimum and a higher quality of channel layer with an extremely low N_{SS} (1.43 × 10^{10} eV^{-1} cm^{-2}). The statistically calculated mean SS of the device was decreased to 87 mV dec^{-1}, which was superior to other reported ones for OFETs manufactured by large-area solution process.[33]

4.1.3 Combination of high capacitance with a low trap density. To further decrease the SS of the device for a high-performance OFET-based transducer, increasing the capacitance and decreasing the sub-gap density of states can be synergistically exploited. For example, Zhao *et al.* reported a steep subthreshold OFET by combining the P(VDF–TrFE–CFE)/PVCN bilayer dielectric and 6,13-bis(triisopropylsilylethynyl)-penta-

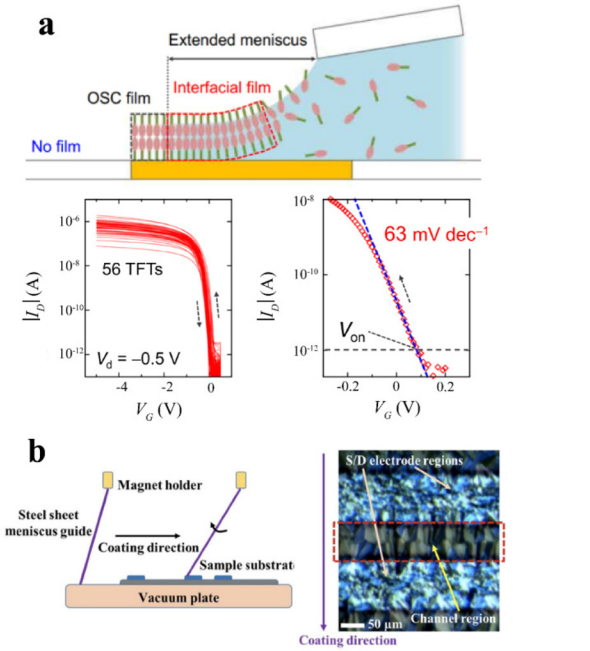

Fig. 6 Decreasing the sub-gap density of states (N_{SS}) at the channel for steep SS. (a) Extended meniscus coating for forming high-quality single crystals onto an inert, hydrophobic CYTOP surface. Reprinted with permission from ref. 5. Copyright 2020, American Association for the Advancement of Science. (b) Process optimization by introducing soft contact coating (SCC) for forming low DOS channels. Reprinted with permission from ref. 33. Copyright 2019, IEEE.

cene/polystyrene blends. The addition of a low-*k* dielectric layer (PVCN) helped to screen the polarization of the P(VDF–TrFE–CFE) layer at a long-term bias, resulting in a smoother channel interface for facilitating carrier transportation compared to the pure P(VDF–TrFE–CFE) layer. The capacitance was increased to 46.3 nF cm^{-2} while the N_{SS} was decreased down to 1.92 × 10^{10} eV^{-1} cm^{-2} eliminating the risk of the stability issue. As a result, the SS was remarkably decreased to 64 mV dec^{-1}, approaching the theoretical limit at room temperature.[126]

Adopting a high-*k* dielectric layer was beneficial for decreasing the SS of the device and increasing the sensitivity, but the polarization of the high-*k* dielectric layer might induce stability issues. To ameliorate the stability issue, another low-*k* dielectric layer was essential for screening the polarization with the sacrifice of high capacitance. In addition, decreasing the N_{SS} was another way to decrease the SS, where a small molecule/polymer blend was mostly taken. It is reasonable to expect that the SS can be remarkably decreased by using a combination of increasing gate capacitance and reducing sub-gap trap density. This is crucial for highly sensitive biochemical sensors as the SS of the OFET device determines the current conversion sensitivity of the transducer. However, in addition to sensitivity, the stability of the OFET device is another key indicator, which determines the precision of the sensing signals. And in the next part, the mechanism of stability and methods for increasing the stability of the device by utilizing nanomaterials will be elaborated.

4.2 Enhancing the stability of OFETs

To maintain the accuracy and reliability of OFET biosensors during operation, excellent stability is also required in addition to a steep SS. However, a few matters could impact the stability of OFETs, such as dielectric polarizability, traps, and defects in the interface (*e.g.* dangling bonds from the oxide dielectric layer and some atmosphere factors). Hence, interface engineering was often used to eliminate trap density by modifying the dielectric surface. SAMs have been utilized to modify the surfaces of oxide dielectric layers to decrease dangling bonds and traps. As reported by Kim *et al.*,[127] a donor–acceptor type liquid-crystalline semiconducting copolymer (PQTBTz-C_{12}) based OFET showed unprecedented bias-stress stability after surface modification with SAMs comparable to that of amorphous silicon, thanks to the reduced concentration of charge traps (Fig. 7a–c). Introducing an amorphous dielectric material with small permittivity between the semiconductor layer and high-*k* dielectric layer is another potential method to reduce the dielectric polarizability and trap concentration.[128] For example, Jia *et al.*[129] reported an exhaustive characterization of OFETs with an ultra-thin bilayer gate dielectric comprising the amorphous fluoropolymer CYTOP and Al_2O_3:HfO_2 nanolaminate. The shift of threshold voltages remained below 0.2 V even over a time period of up to 5.9 × 10^5 s with filed-effect carrier mobility of up to 1.6 cm^2 V^{-1} s^{-1}. However, the use of a polymer dielectric and interlayer is preferred so that OFET devices are feasible to being fully solution-processed. By adding a thin CYTOP layer between the P(VDF–TrFE–CFE) layer and the semiconductor layer, the OFET developed by Tang *et al.* showed that the charge trapping in the channel and accumulation by remanent polarization under the gate bias was able to neutralize with each other.[130] As a result, the resulting OFET showed negligible hysteresis and excellent negative bias stressing stability (Fig. 7d and e).

5. Hybrid integration of OFET biochemical sensors

The sensitivity and reliability of OFET biochemical sensors can be improved by both sensing interface and device engineering as mentioned before. Besides, it is requested integration of the transducer and SEs into the biochemical sensor to make it easy for sensing applications. OFET biochemical sensors have been widely demonstrated in the detection of various ions and biomolecules by modifying different sensing active materials on the extended gate.[30,31] Table 2 presents a summary of OFET-based biosensors for various biochemical targets by employing SE modified with different sensitive layers. Here, recent efforts in the integration of OFET biochemical sensors and portable sensing systems are reviewed and discussed.

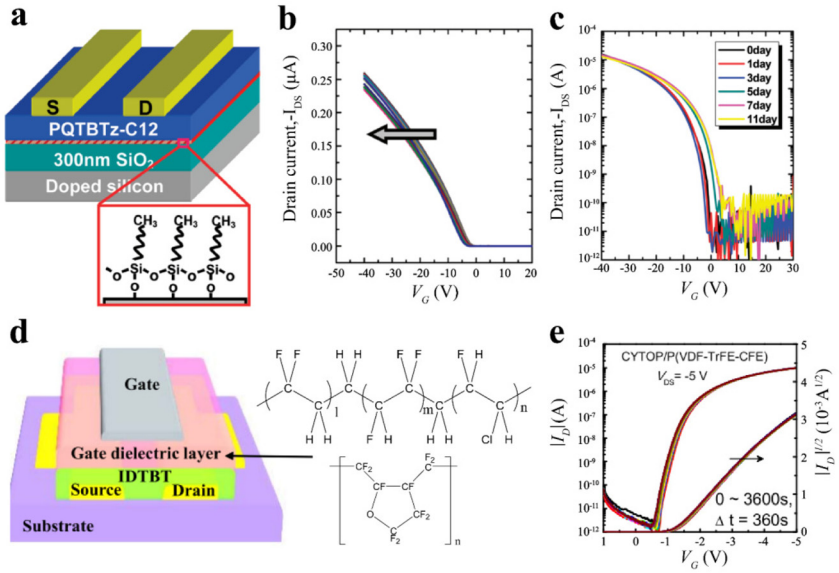

Fig. 7 Interface engineering of high stability OFETs. (a) Schematic side-view of the transistor and a chemical representation of the OTS interlayer used as a modification layer. (b) Linear transfer curves of the PQTBTz-C12-based OFET as a function of stress time annealed at 180 °C and (c) air stability of the PQTBTz-C12-based OFET. Reprinted with permission from ref. 127. Copyright 2009, American Chemical Society. (d) Schematic of the device structure of the top gate bottom contact OFET using different gate dielectric layers: the single layer CYTOP, single layer relaxor ferroelectric terpolymer P(VDF–TrFE–CFE), and CYTOP/P(VDF–TrFE–CFE) bilayer. (e) I_D–V_{GS} curves were measured at different times under negative bias stress (NBS) at V_{GS} = −5 V, V_{DS} = −5 V for the bilayer OFET. Reprinted with permission from ref. 130. Copyright 2017, IEEE.

5.1 Proof-of-concept sensing enabled by wire connection

To ensure the stability of the OFET performance, biochemical sensors of OFETs were usually reassembled by connecting individual OFETs and SEs *via* conductive wire, as illustrated in Fig. 8. This discrete integration method offers a simple set-up process for EGOFET biochemical sensors without considering process compatibility issues. Zhao *et al.*[131] reported a pH ISOFET by combining the H^+ sensitive ITO electrode as the extended gate with a printed low-voltage OFET. When operated in the highly sensitive subthreshold regime (SS < 83 mV dec^{-1}), the ISOFET sensor could detect pH variations less than 0.1. By replacing the conductive wire with a planar gold film electrode, a taurine sensor was developed by using a MIP-modified Au SE as the extended gate of a printed OFET transducer.[37] The OFET sensor exhibited excellent selectivity due to the high specific affinity of MIPs for taurine. By changing the materials modified on SEs, the sensor could also be applied in the detection of heavy metal ions,[18,19,132] electrolyte ions,[32,133–135] protein[39,136,137] and small biomolecules,[35,138–140] *etc*. Currently reported OFET biochemical sensors are mainly based on this format, namely combining OFET devices with different SEs for achieving signal responses to various biochemical analytes. However, this type of testing is only for material characterization or a proof-of-concept for detection, which is far away from the design of sensing chips. For on-site applications, it is necessary to integrate an OFET biochemical sensor into a miniaturized sensing chip or a sensing tag of a fairly large area.

5.2 Advanced integration of a sensing chip

5.2.1 On-chip packaging. As shown in Fig. 9a, on-chip packaging free of external connections is a routine way for the integration of a solid-state OFET biochemical sensor. Li and co-workers developed a fully integrated pH sensing tag on a plastic substrate, which comprised a pH-sensitive ITO electrode, a low-voltage printed OFET, and a solid-state Ag/AgCl/PVB thin film RE (Fig. 9b).[41] This sensing tag was demonstrated to readout by a handheld readout system and present reliable pH monitoring in Bluetooth connected smartphones. Similarly, Tang *et al.*[29] established flexible integrated label-free miRNA sensing tags based on printed low-voltage OFET devices. The steep SS makes OFET with a high transconductance efficiency (g_m/I_D) and presents a large signal-to-noise. The EGOFET biosensor tag presented high sensitivity and achieved the detection limit up to the 10 pM level with a low operation voltage (<1 V).

Another advantage of on-chip packaging is to realize multichannel transistor-based biochemical sensors for the multiplex detection of analytes. Huang *et al.*[33] constructed a fully integrated multiplexed sensing tag consisting of three solution-processed low-voltage OFETs, solid-state Na^+, K^+, and H^+ ISEs and a solid-state RE on a flexible thin film substrate (Fig. 9c). This integrated sensing tag was low-voltage powered so that it could be used in handheld three channel readout systems controlled by a Bluetooth connected smartphone, presenting reliable monitoring of the concentrations of Na^+, K^+ and H^+ in solutions. The bonding process of individual components on the same substrate may also impact the reliability

Table 2 Summary of solution-printed OFET-based biochemical sensors

Sensor type	Sensitive material	Target	SS (mV dec^{-1})	$\lvert V_{GS}\rvert$ (V)	Linear ranges	Limit of detection	Ref.
EGOFET	Antibody	Glial fibrillary acidic protein	880[a]	<2	0.5–100 ng ml^{-1}	1 ng ml^{-1}	141
EGOFET	Antibody	C-reactive protein	180[a]	<3	0.5–10 μg ml^{-1}	1 μg ml^{-1}	15
EGOFET	Cu^{2+}–DPA	HPO_4^{2-}	NR	<1	9–129 μM	NR	134
EGOFET	Zn^{2+}–DPA	Phosphate anions	NR	<1	0–100 μM	NR	135
EGOFET	Zn^{2+}–DPA	Phosphoprotein (α-casein)	NR	<1	0–6 μM	0.22 ppm	38
EGOFET	Horseradish peroxidase/ diamine oxidase	Histamine	870[a]	<3	0–10 μM	1.2 μM	136
EGOFET	Anti-IgA-antibody	IgA	880[a]	<3	0–10 μM	NR	142
EGOFET	Streptavidin	Biotinylated IgG	320[a]	<3	0–10 μg mL^{-1}	1.2 μg mL^{-1} (8 nM)	143
EGOFET	Nitrilotriacetic acid (NTA)	Cu^{2+}	NR	<1	0–15 μM	0.51 μM (96 ppb)	19
EGOFET	Cysteine	Hg^{2+}	NR	<1	0–0.5 μM	31 ppb	132
EGOFET	Glucose oxidase/Prussian blue	Glucose	135[a]	<3	0–51.2 mM	NR	35
EGOFET	Molecularly imprinted polymers	Taurine	NR	<3	0–10 μM	0.33 μM	37
EGOFET	Molecularly imprinted polymers	(*S*)-Hyoscyamine	NR[a]	<3	0–100 μM	NR	86
EGOFET	SH-DNA	miRNA	80	<1	10 pM–1 mM	10 pM	29
EGOFET	ITO	pH	195[a]	<3	pH 4–10	NR	41
3-Channels EGOFET	Na^+ ISM K^+ ISM ITO	Na^+ K^+ pH	80	<3	1–80 mM 1–128 mM pH 4–10	1 mM 1 mM pH 10	33
4-Channels EGOFET	PANI	pH	100	<3	pH 9–6	pH 9	144
Dual gate EGOFET	Anti-IgG-antibody	IgG	637 ± 72	<10	0–10 μg mL^{-1}	NR	39
EGOFET amplifier	K^+-ISM	K^+	80[a]	<3	1–64 mM	NR	32
EGOFET amplifier	Lactate oxidase	Lactate	2500[a]	<10	20–60 mM	NR	36
EGOFET amplifier	Lactate oxidase	Lactate	100[a]	<4	0–0.5 mM	NR	138
EGOFET amplifier	ITO	pH	110	<3	pH 7.2–7.4	NR	40

EGOFET: extended-gate type OFET. [a] Data calculated from the reported information; NR: not reported.

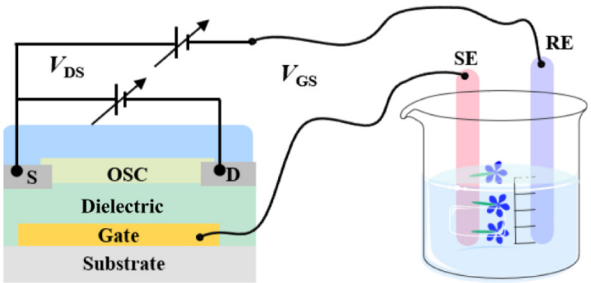

Fig. 8 OFET biochemical sensing enabled by wire connection, consisting of an OFET, a sensing electrode (SE), a reference electrode (RE) and analytes.

performance of the OFETs, for example, volatilization of the adhesive solvent, bonding temperature, *etc*. To solve this, Tang *et al.*[34] proposed a low-temperature (<85 °C) packaging approach with a hollow structure to release the affecting solvents. The packaged OFETs exhibited excellent stability even after 24 days of storage under atmospheric conditions. Although on-chip packaging is highly flexible and customizable, the resulting biochemical sensors may suffer from poor mechanical stability, low-density integration, and high noise.

5.2.2 Three-dimensional (3D) integration. OFET biochemical sensors can be stacked vertically in a 3D integration by connecting the sensing portion and transistor transducer through a via hole (Fig. 10a). This kind of integration will increase the density of the advanced OFET biochemical sensor chip, and the through-hole connection reduces the length of the connection lines, thus suppressing external noise. Han *et al.*[40] proposed a through-plastic-via (TPV) 3D integration method for pH ISOFET sensing chips (Fig. 10b–d). They fabricated separate arrays of OFET circuits and sensing elements on different substrates, which were then stacked back-to-back to form the electrical interconnects of the TPV. The full solution printed flexible OFET amplifier circuitry array presented excellent operational stability and exhibited a voltage gain larger than 10 at V_{DD} = 5 V. Due to the high voltage gain of the OFET amplifier, the sensitivity of the integrated pH sensor was increased from 35 mV per pH to 400 mV per pH, which was nearly 11 times higher. Because TPV 3D integration enabled the OFET ampli-

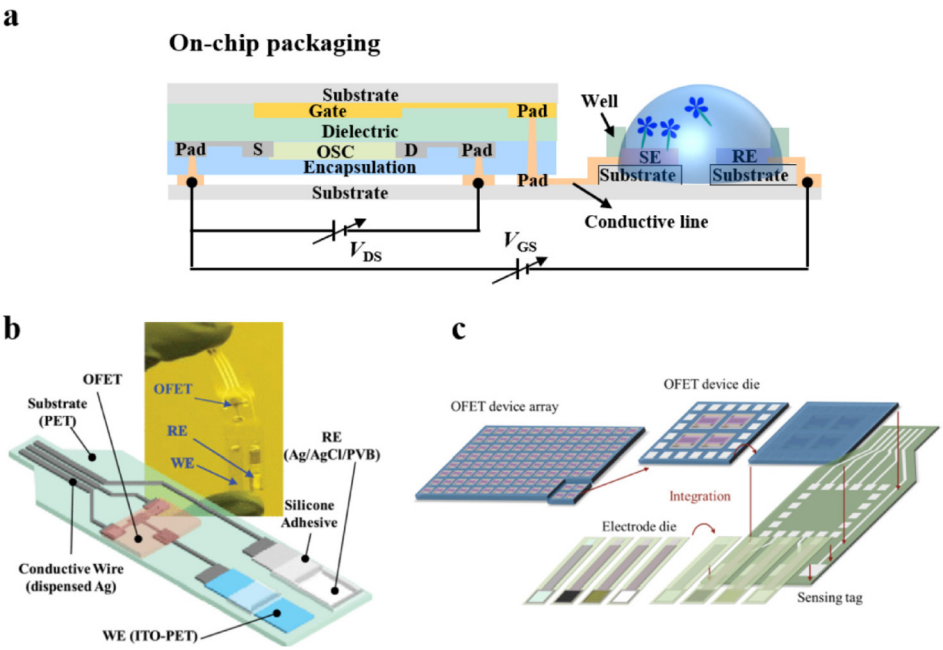

Fig. 9 On-chip packaging for the integration of OFET biochemical sensors. (a) Cross-sectional structure of an integrated OFET biochemical sensor chip enabled by on-chip packaging, which assembles the OFET, SE and RE on the same carrier substrate. (b) Photo image and illustration diagram for the flexible pH ISOFET tag integrated on one plastic. Reprinted with permission from ref. 130. Copyright 2017, IEEE. (c) Illustration of the integration process for building an array of multiplexed ISOFETs. Reprinted with permission from ref. 33. Copyright 2019, IEEE.

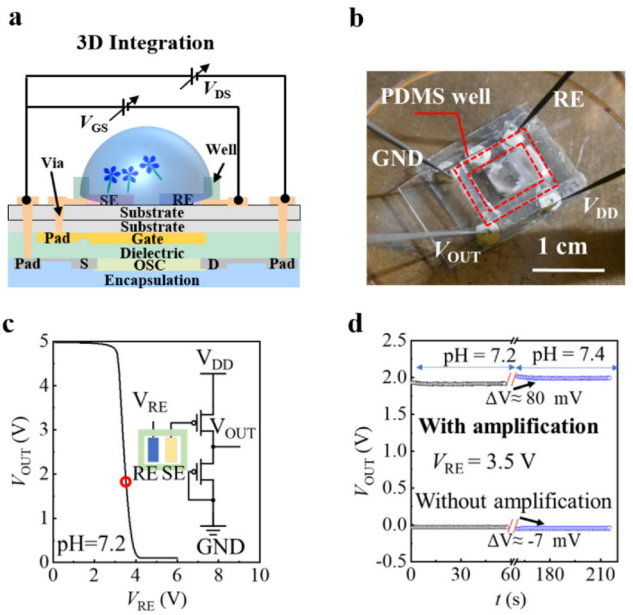

Fig. 10 3D integration of the OFET biochemical sensor chip. (a) Cross-sectional structure of the 3D integrated OFET biochemical sensor chip, which stacks the OFET with a sensing portion and is connected through a via hole. (b) Photo image of the 3D integrated pH sensor chip based on OFET amplifier circuitry. (c) The schematic structure and the measured transfer curves (V_{OUT}–V_{RE}) of the integrated biochemical sensor. (d) Comparison of pH responses with and without OFET amplifier circuitry. Reprinted with permission from ref. 40. Copyright 2021, IEEE.

fier to be made close to the SE and RE, it was useful to suppress the influence of external noise and improve the signal-to-noise ratio of the biosensor. 3D integration of the OFET biochemical sensor chip has advantages such as increased density, suppressed signal noise, and high robustness. However, the remaining issues would be the risk of alignment difficulties and mismatching between the two sets of substrate units for transducers and SE/RE arrays, respectively.

5.2.3 Monolithic integration. Monolithic integration tries to manufacture individual components on a single substrate, eliminating the need for manual assembly, which enables reliable interconnection and a smaller footprint. The main challenge for monolithically integrating SEs with OFETs remains to be the processing compatibility of material stacking. The sensing material is modified on the gate to form an SE, which means that the gate needs to have a certain area exposed to immobilization and sensing (Fig. 11a). OFETs with a bottom gate structure require the patterning of dielectrics, OSC layers, and even encapsulation layers, resulting in more complexity of the process. Therefore, it is better to choose OFETs with a top gate for the construction of monolithically integrate OFET biochemical sensors. On this basis, Minamiki *et al.* constructed an ultra-thin (1 μm) dual-gate OFET-based flexible immunosensor chip with a monolithic integration structure (Fig. 11b–d).[39] The extended Au top gate was functionalized by the antibody, which had high affinity for immunoglobulin G (IgG). The mechanical durability test showed that with a stress of 15%, the developed flexible OFET sensor

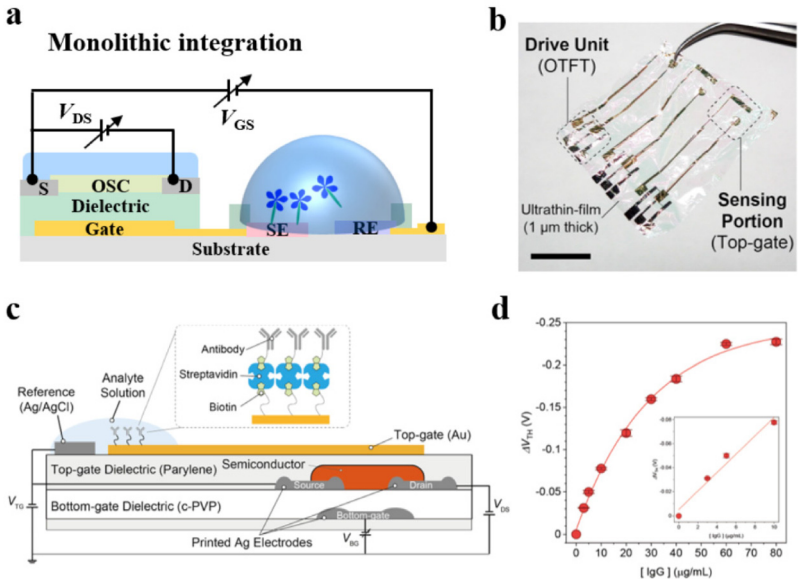

Fig. 11 Monolithic integration of the OFET biochemical sensor chip. (a) Cross-sectional structure of the monolithically integrated ISOFET. (b) Photos and (c) schematic diagram of the monolithically integrated ultra-thin OFET immunosensor. The top gate was immobilized with anti-IgG antibodies. (d) Changes in the threshold voltage (V_{th}) of the OFET-based immunosensor induced by detection of IgG protein in PBS solution. Reprinted with permission from ref. 39. Copyright 2021 Springer Nature.

showed stable operation performance, indicating great potential in wearable biochemical sensing applications.

5.3 Demonstration of system integration

Printable OFETs are very promising for developing physical and chemical sensors for the assembly of customized sensory systems. Nevertheless, entirely printed OFET technology cannot realize all the functions such as accurate analog-to-digital conversion (ADC), complex signal processing, power management, or wireless communication. For the envisioned applications, hybrid technology has been thus proposed to combine organic functional devices with silicon chips.[145,146] There is a window for printable OFETs to realize interface circuits and process local signals. In this sense, OFET amplifiers are crucial to enable the front-end organic sensors to interface with peripheral readout systems.[147] This retains the benefits of solution-process and printing without sacrificing the device performance, representing the future development direction in this field.

Based on low voltage printed OFET inverters and amplifiers, a series of fully printable sensor systems for biochemical detection have been demonstrated. For instance, Feng *et al.* fabricated an ammonia sensing tag based on a high air stability OFET. It can reliably sense ammonia in the range of 5 to 25 ppb over a long period.[148] The OFET sensing tag showed the excellent features of low voltage and stable operation, which enabled it to be integrated into the self-designed electronic system powered by a 3.7 V lithium-battery, and operated for a long time with a low power consumption as low as 50 nW. Later, Tang *et al.* developed a zero-V_{GS} inverter-based amplifier for the amplification of pH signals, which was composed of an extended-gate pH-sensitive OFET and a loaded OFET.[16] The developed sensing tag on plastic interfaced with a 3.3 V battery-powered readout circuit board, which communicated with a mobile phone through NFC, and showed good linearity over a wide pH range from 2 to 12. In addition to the detection of ions, Nagamine *et al.* reported an enzyme sensor for L-lactate using a printed organic inverter circuit (Fig. 12a).[140] The concentration of L-lactic acid was finally reflected in a color change of the electrophoretic display, which could be read out using the naked eye. This biochemical sensing system presents a portable sensing-driven display and has great potential for application in wearable sensing devices.

For multiplex sensing systems, Huang *et al.*[33] constructed a three-channel ISOFETs sensor array tag for H^+, Na^+, and K^+ detection. The signal was processed by a handheld readout circuit board and sent to the mobile phone by Bluetooth. A handheld 3.3 V battery powered multi-ion sensing system was demonstrated for the point-of-care test. They also developed a versatile flexible hybrid integration (FHI) system that combined the ISOFET technology with an radio frequency identification device (RFID) integrated circuit with a passive power supply.[144] The frame and the system image are shown in Fig. 12b. The four-channel outputs of the FHI system were read out by the smartphone with randomly bending of the key device area 20 times, showing negligible changes, indicating that both the intrinsic OFET part and the external connections in the FHI system had good enough mechanical reliability. With high customization in function, form factor, and cost, the FHI system was regarded as promising for a wide range of applications such as medical diagnostics, chemical or biological process monitoring, and daily health care.

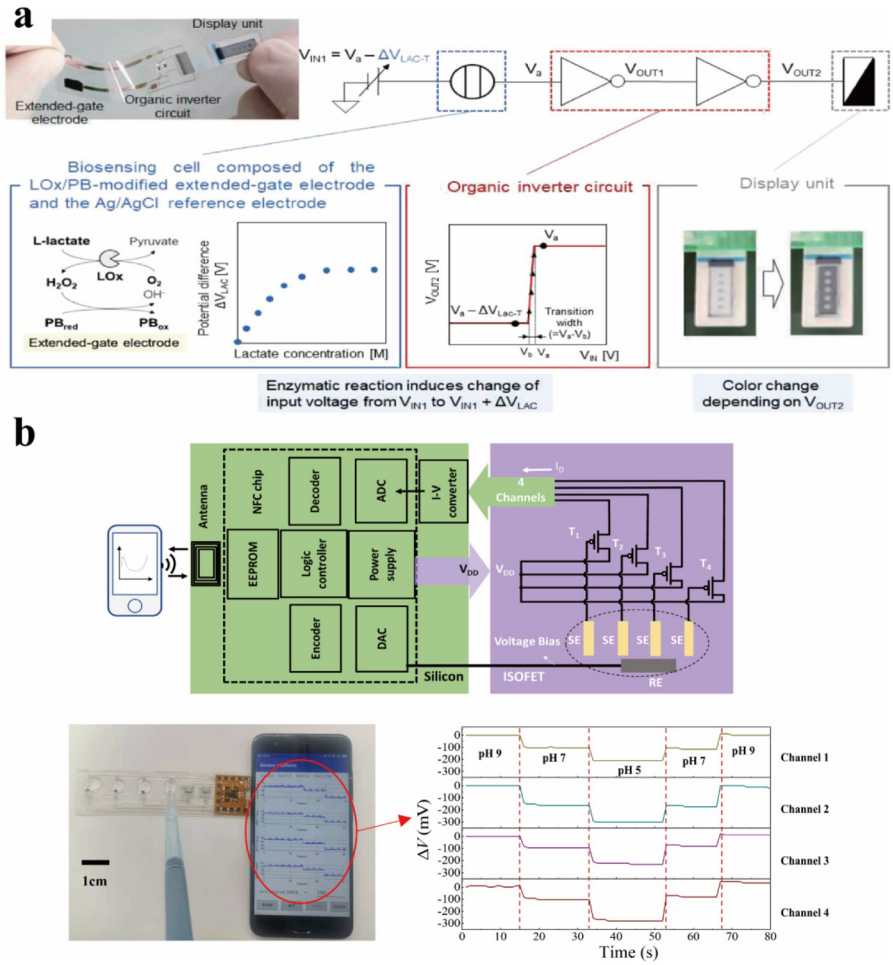

Fig. 12 Integrated OFET biochemical sensing system. (a) Photograph of the printed organic inverter-circuit-based biosensor prototype device with the display unit and its configuration, composed of a biosensing cell composed of the extended-gate and Ag/AgCl reference electrodes, a two-stage organic transistor-based inverter circuit with a p-type semiconductor, and a display unit. Reprinted with permission from ref. 140. Copyright 2019, MYU Scientific Publishing Division. (b) The frame and image of a versatile FHI system combining ISOFET technology and an RFID IC with a passive power supply for diverse bio-sensing. Reprinted with permission from ref. 144. Copyright 2021, IEEE.

6. Conclusions and outlook

6.1 Conclusions

In summary, material and device engineering have been gradually explored to enhance the transduction efficiency of printable OFET transducers and the sensing properties of working electrodes. In this review, approaches to ameliorate the sensitivity and stability of OFET biochemical sensors were described. The sensing performance of the OFET biochemical sensor depended on the performance of OFETs and SEs. On one hand, as an electrical signal transducer, the voltage–current conversion capability of the OFET device is related to the sensitivity of the biochemical sensor. Reducing the SS of OFET devices can improve the sensitivity of OFET biochemical sensors, which can be achieved by increasing the C_{diel} and decreasing the effective N_{SS}. On the other hand, nanomaterials endow the SEs with superb sensitivity, excellent robustness, outstanding reproducibility, and extraordinary competitiveness. Noble metal nanomaterials and metal oxide nanomaterials expand the specific surface area and catalytic effect. Carbon nanomaterials improve the electrical conductivity and enrich binding sites. Organic nanomaterials with rich functional groups not only protect the activity of natural biomolecules but also act as receptors for biochemical target analytes. By combining OFETs with nanomaterial-modified SEs, EGOFET biochemical sensors have been constructed for a wide range of analytes. With advanced integration strategies, OFET biochemical sensors can be integrated into portable sensing tags or sensing chips, representing great potential for portable or wearable sensing instruments. Nevertheless, hybrid integration of printable OFET biochemical sensor tags or chips with a silicon-based portable readout system is a promising approach for the construction of portable, wearable, and implantable devices in future applications.

6.2 Outlook

Although considerable progress has been made, the development of OFET biochemical sensors is still at the stage of lab-

oratory validation, and there are many challenges to be overcome in terms of practical applications or the launch of commercial products.

6.2.1 Scalable integration. For the miniaturization of OFET biochemical sensors, the main limits may be the miniaturization of SEs and REs in the sensing portion. The miniaturized solid-state SEs have been reported with various functions but the research on REs is insufficient. As REs are requied to provide a stable interface potential for the sensing system, their stability are very important for the overall stability of the sensing chip, and their miniaturization also affect the integration density of the chip.[41,149] The manufacture of miniaturized solid state REs with high stability during measurement is essential for the integration of OFET sensing chips.

6.2.2 High throughput multiplex sensing in arrays. One advantage of the OFET biochemical sensor is its great potential for multiple sensing with array circuits. This is very attractive for biochemical analysis as different indicators often need to be measured simultaneously to draw reliable conclusions and mitigate false results. For the application of multiplexed sensing arrays, the uniformity and repeatability of OFET biochemical sensors need to be addressed, and low-cost, high-throughput manufacturing needs to be achieved. In this regard, Guo's group has been working on the exploration of multi-channel OFET sensing arrays. With the development of the soft-contact coating method, the fabrication of high throughput OFET arrays presents excellent uniformity.[12] Based on this, they have realized the construction of multi-channel ISOFET array tags.[33,34,144] However, the results reported so far are mainly based on discrete integration of OFETs with SEs and REs, which leads to low density and poor robustness of the integrated chip and is not suitable for large-scale array production. The development of high throughput multiplexed sensing chips based on monolithic integration may be the way forward for sensing arrays.

6.2.3 Integration of microfluidic platforms. The development of microfluidic technology leads to the evolution of biochemical analytical procedures.[150] The introduction of microfluidic systems in other electrochemical sensors has already brought significant benefits, such as greatly reduced sample volumes and the convenience of continuous and rapid *in situ* measurement of targets,[88,151] especially for multi-sensor arrays.[152] However, there are few reports on the introduction of microfluidic platforms into OFET biochemical sensors. This may be due to the fact that most OFET sensor chips are assembled based on discrete components, limiting their integration with microfluidic systems. The design of OFET biochemical sensor chips that are well-matched to microfluidic systems is vital for their future development in practical applications.

Conflicts of interest

There are no conflicts to declare.

Acknowledgements

This work was supported by the Shanghai Science and Technology Commission (Grant No. 19JC14122400), the National Science Fund for Excellent Young Scholars under Grant (61922057) and the National Natural Science Foundation of China (61974091).

References

1 A. Tsumura, H. Koezuka and T. Ando, *Appl. Phys. Lett.*, 1986, **49**, 1210–1212.
2 A. C. Arias, J. D. MacKenzie, I. McCulloch, J. Rivnay and A. Salleo, *Chem. Rev.*, 2010, **110**, 3–24.
3 J. Li, Z. Sun and F. Yan, *Adv. Mater.*, 2012, **24**, 88–93.
4 M. Kunii, H. Iino and J.-I. Hanna, *IEEE Electron Device Lett.*, 2016, **37**, 486–488.
5 G. Kitahara, S. Inoue, T. Higashino, M. Ikawa, T. Hayashi, S. Matsuoka, S. Arai and T. Hasegawa, *Sci. Adv.*, 2020, **6**, eabc8847.
6 S. Gamerith, A. Klug, H. Scheiber, U. Scherf, E. Moderegger and E. J. W. List, *Adv. Funct. Mater.*, 2007, **17**, 3111–3118.
7 C. Kim, Z. M. Wang, H. J. Choi, Y. G. Ha, A. Facchetti and T. J. Marks, *J. Am. Chem. Soc.*, 2008, **130**, 6867–6878.
8 J. Kwon, S. Baek, Y. Lee, S. Tokito and S. Jung, *Langmuir*, 2021, **37**, 10692–10701.
9 S. Conti, S. Lai, P. Cosseddu and A. Bonfiglio, *Adv. Mater.*, 2017, **2**, 1600212.
10 J. H. Cho, J. Lee, Y. Xia, B. Kim, Y. He, M. J. Renn, T. P. Lodge and C. Daniel Frisbie, *Nat. Mater.*, 2008, **7**, 900–906.
11 S. Lee, A. Reuveny, J. Reeder, S. Lee, H. Jin, Q. Liu, T. Yokota, T. Sekitani, T. Isoyama, Y. Abe, Z. Suo and T. Someya, *Nat. Nanotechnol.*, 2016, **11**, 472–478.
12 Y. Huang, W. Tang, S. Chen, L. Han, X. Hou and X. Guo, *IEEE Electron Device Lett.*, 2019, **40**, 1945–1948.
13 F. A. Viola, J. Barsotti, F. Melloni, G. Lanzani, Y. H. Kim, V. Mattoli and M. Caironi, *Nat. Commun.*, 2021, **12**, 5842.
14 E. Stucchi, A. D. Scaccabarozzi, F. A. Viola and M. Caironi, *J. Mater. Chem. C*, 2020, **8**, 15331–15338.
15 X. Ji, P. Zhou, L. Zhong, A. Xu, A. C. O. Tsang and P. K. L. Chan, *Adv. Sci.*, 2018, **5**, 1701053.
16 W. Tang, C. Jiang, Q. Li, W. Hu, L. Feng, Y. Huang, J. Zhao, S. Chen and X. Guo, *IEEE Electron Device Lett.*, 2016, **37**, 1002–1005.
17 X. Wu, J. Zhou and J. Huang, *Macromol. Rapid Commun.*, 2018, **39**, e1800084.
18 T. Minami, Y. Sasaki, T. Minamiki, P. Koutnik, P. Anzenbacher, Jr. and S. Tokito, *Chem. Commun.*, 2015, **51**, 17666–17668.
19 Y. Sasaki, T. Minami, T. Minamiki and S. Tokito, *Electrochemistry*, 2017, **85**, 775–778.

20 C. Bartic, B. Palan, A. Campitelli and G. Borghs, *Sens. Actuators, B*, 2002, **83**, 115–122.
21 L. Kergoat, B. Piro, M. Berggren, M.-C. Pham, A. Yassar and G. Horowitz, *Org. Electron.*, 2012, **13**, 1–6.
22 S. Lai, M. Demelas, G. Casula, P. Cosseddu, M. Barbaro and A. Bonfiglio, *Adv. Mater.*, 2013, **25**, 103–107.
23 C. Napoli, S. Lai, A. Giannetti, S. Tombelli, F. Baldini, M. Barbaro and A. Bonfiglio, *Sensors*, 2018, **18**, 990.
24 R. Kubota, Y. Sasaki, T. Minamiki and T. Minami, *ACS Sens.*, 2019, **4**, 2571–2587.
25 T. Minami, T. Minamiki and Y. Sasaki, *Electrochemistry*, 2018, **86**, 303–308.
26 T. Minami, *J. Inclusion Phenom. Macrocyclic Chem.*, 2021, **101**, 1–18.
27 K. Nagamine, A. Nomura, Y. Ichimura, R. Izawa, S. Sasaki, H. Furusawa, H. Matsui and S. Tokito, *Anal. Sci.*, 2020, **36**, 291–302.
28 K. Nagamine and S. Tokito, *Sens. Actuators, B*, 2021, **349**, 130778.
29 W. Tang, Y. Fu, Y. Huang, Y. Li, Y. Song, X. Xi, Y. Yu, Y. Su, F. Yan and X. Guo, *npj Flexible Electron.*, 2022, **6**, 1–8.
30 T. Nguyen, Y. Seol and N.-E. Lee, *Org. Electron.*, 2011, **12**, 1815–1821.
31 T. Ji, P. Rai, S. Jung and V. K. Varadan, *Appl. Phys. Lett.*, 2008, **92**, 208.
32 R. Shiwaku, H. Matsui, K. Nagamine, M. Uematsu, T. Mano, Y. Maruyama, A. Nomura, K. Tsuchiya, K. Hayasaka, Y. Takeda, T. Fukuda, D. Kumaki and S. Tokito, *Sci. Rep.*, 2018, **8**, 1–8.
33 Y. Huang, Y. Song, Y. Tang, Z. Liu, L. Han, Q. Zhang, B. Ouyang, W. Tang, L. Feng and X. Guo, presented in part at the 2019 IEEE Int. Electron Devices Meeting (IEDM), 2019, pp. 18.5.1–18.5.4.
34 Y. Tang, W. Tang, Y. Song, L. Han, Y. Huang, R. Liu, Y. Su and X. Guo, *IEEE J. Electron Devices Soc.*, 2021, **9**, 1237–1242.
35 T. Mano, K. Nagamine, Y. Ichimura, R. Shiwaku, H. Furusawa, H. Matsui, D. Kumaki and S. Tokito, *ChemElectroChem*, 2018, **5**, 3881–3886.
36 S. Baek, J. Kwon, T. Mano, S. Tokito and S. Jung, *Macromol. Biosci.*, 2020, **20**, e2000144.
37 Q. Zhou, M. Wang, S. Yagi and T. Minami, *Nanoscale*, 2021, **13**, 100–107.
38 T. Minamiki, T. Minami, P. Koutnik, P. Anzenbacher, Jr. and S. Tokito, *Anal. Chem.*, 2016, **88**, 1092–1095.
39 T. Minamiki, T. Minami, Y. P. Chen, T. Mano, Y. Takeda, K. Fukuda and S. Tokito, *Commun. Mater.*, 2021, **2**, 1–8.
40 L. Han, S. Chen, L. Deng, Y. Song, Y. Huang, S. Li, M. Li, W. Tang, Y. Su and X. Guo, *IEEE Electron Device Lett.*, 2021, **42**, 569–572.
41 Q. Li, J. Zhao, Y. Huang, W. Tang, S. Peng, S. Qiu, Q. Zhang and X. Guo, *IEEE Electron Device Lett.*, 2018, **39**, 591–594.
42 S. J. Kwon and A. J. Bard, *J. Am. Chem. Soc.*, 2012, **134**, 10777–10779.
43 L. Kong, S. Lv, Z. Qiao, Y. Yan, J. Zhang and S. Bi, *Biosens. Bioelectron.*, 2022, **207**, 114188.
44 X. Li, K. Ren, M. Zhang, W. Sang, D. Sun, T. Hu and Z. Ni, *Sens. Actuators, B*, 2019, **293**, 122–128.
45 F. Haghayegh, R. Salahandish, M. Hassani and A. Sanati-Nezhad, *ACS Appl. Mater. Interfaces*, 2022, **14**, 10844–10855.
46 R. Marega, F. De Leo, F. Pineux, J. Sgrignani, A. Magistrato, A. D. Naik, Y. Garcia, L. Flamant, C. Michiels and D. Bonifazi, *Adv. Funct. Mater.*, 2013, **23**, 3173–3184.
47 Y. Song, M. Zhao, H. Li, X. Wang, Y. Cheng, L. Ding, S. Fan and S. Chen, *Sens. Actuators, B*, 2018, **255**, 1927–1936.
48 M. Mohammadniaei, A. Go, S. G. Chavan, A. Koyappayil, S. E. Kim, H. J. Yoo, J. Min and M. H. Lee, *Biosens. Bioelectron.*, 2019, **141**, 111468.
49 Z. Jiang, X. Xi, S. Qiu, D. Wu, W. Tang, X. Guo, Y. Su and R. Liu, *J. Mater. Sci.*, 2019, **54**, 13674–13684.
50 M. Chen, Z. Song, X. Yang, Z. Song and X. Luo, *Biosens. Bioelectron.*, 2022, **206**, 114162.
51 Z. Song, R. Li, X. Yang, Z. Zhang and X. Luo, *Sens. Actuators, B*, 2022, **367**, 132110.
52 J. Kim, I. Jeerapan, J. R. Sempionatto, A. Barfidokht, R. K. Mishra, A. S. Campbell, L. J. Hubble and J. Wang, *Acc. Chem. Res.*, 2018, **51**, 2820–2828.
53 C. Sun, X. Wang, M. A. Auwalu, S. Cheng and W. Hu, *EcoMat*, 2021, **3**, e12094.
54 G. Palazzo, D. De Tullio, M. Magliulo, A. Mallardi, F. Intranuovo, M. Y. Mulla, P. Favia, I. Vikholm-Lundin and L. Torsi, *Adv. Mater.*, 2015, **27**, 911–916.
55 D. Wang, V. Noël and B. Piro, *Electronics*, 2016, **5**, 9.
56 P. Estrela, V. Pachauri and S. Ingebrandt, *Essays Biochem.*, 2016, **60**, 81–90.
57 W. Tang, Y. Huang, L. Han, R. Liu, Y. Su, X. Guo and F. Yan, *J. Mater. Chem. C*, 2019, **7**, 790–808.
58 Y. S. Rim, S. H. Bae, H. Chen, N. De Marco and Y. Yang, *Adv. Mater.*, 2016, **28**, 4415–4440.
59 Y. Khan, A. Thielens, S. Muin, J. Ting, C. Baumbauer and A. C. Arias, *Adv. Mater.*, 2020, **32**, e1905279.
60 T. Kant, K. Shrivas, K. Dewangan, A. Kumar, N. K. Jaiswal, M. K. Deb and S. Pervez, *Mater. Today Chem.*, 2022, **24**, 100769.
61 H. Li, W. Shi, J. Song, H. J. Jang, J. Dailey, J. Yu and H. E. Katz, *Chem. Rev.*, 2019, **119**, 3–35.
62 B. M. Lowe, K. Sun, I. Zeimpekis, C. K. Skylaris and N. G. Green, *Analyst*, 2017, **142**, 4173–4200.
63 J. Song, J. Dailey, H. Li, H. J. Jang, P. Zhang, J. T. H. Wang, A. D. Everett and H. E. Katz, *Adv. Funct. Mater.*, 2017, **27**, 1606506.
64 N. C. Vieira, A. Figueiredo, A. D. Faceto, A. A. de Queiroz, V. Zucolotto and F. E. Guimarães, *Sens. Actuators, B*, 2012, **169**, 397–400.
65 J. Wu, C. Yu, Y. Yu, J. Chen, C. Zhang, R. Gao, X. Mu, Y. Geng and J. He, *Sens. Actuators, B*, 2020, **305**, 127280.

66 Y. Song, M. Zhao, X. Wang, H. Qu, Y. Liu and S. Chen, *Mater. Chem. Phys.*, 2019, **234**, 217–223.
67 Q. Zhai, L. W. Yap, R. Wang, S. Gong, Z. Guo, Y. Liu, Q. Lyu, J. Wang, G. P. Simon and W. Cheng, *Anal. Chem.*, 2020, **92**, 4647–4655.
68 W. Tang, Z. Wang, J. Yu, F. Zhang and P. He, *Anal. Chem.*, 2018, **90**, 8337–8344.
69 S. Wang, Y. Wu, Y. Gu, T. Li, H. Luo, L. H. Li, Y. Bai, L. Li, L. Liu, Y. Cao, H. Ding and T. Zhang, *Anal. Chem.*, 2017, **89**, 10224–10231.
70 S. Zhao, C. Shi, H. Hu, Z. Li, G. Xiao, Q. Yang, P. Sun, L. Cheng, W. Niu, J. Bi and Z. Yue, *Biosens. Bioelectron.*, 2020, **151**, 111962.
71 X. Hong, H. Wu, C. Wang, X. Zhang, C. Wei, Z. Xu, D. Chen and X. Huang, *ACS Appl. Mater. Interfaces*, 2022, **14**, 9644–9654.
72 R. Abedi, J. Bakhsh Raoof, A. Bagheri Hashkavayi and M. Asghary, *Microchem. J.*, 2021, **170**, 106668.
73 R. Del Caño, T. García-Mendiola, D. García-Nieto, R. Álvaro, M. Mónica, H. A. Iniesta, R. Coloma, C. R. Diaz, P. Milán-Rois, M. Castellanos, M. Abreu, R. Cantón, J. C. Galán, T. Pineda, F. Pariente, R. Miranda, A. Somoza and E. Lorenzo, *Microchim. Acta*, 2022, **189**, 1–12.
74 Y. Zhou, J. Liu, H. Dong, Z. Liu, L. Wang, Q. Li, J. Ren, Y. Zhang and M. Xu, *Biosens. Bioelectron.*, 2022, **203**, 114042.
75 H. Li, B. Kou, Y. Yuan, Y. Chai and R. Yuan, *Biosens. Bioelectron.*, 2022, **197**, 113758.
76 M. Elfiky, N. Salahuddin and A. Matsuda, *Mater. Sci. Eng., C*, 2020, **111**, 110773.
77 T. Dayakar, K. Venkateswara Rao, K. Bikshalu, V. Malapati and K. K. Sadasivuni, *Biosens. Bioelectron.*, 2018, **111**, 166–173.
78 M. Mohammadniaei, A. Koyappayil, Y. Sun, J. Min and M. H. Lee, *Biosens. Bioelectron.*, 2020, **159**, 112208.
79 L. Fabiani, M. Saroglia, G. Galata, R. De Santis, S. Fillo, V. Luca, G. Faggioni, N. D'Amore, E. Regalbuto, P. Salvatori, G. Terova, D. Moscone, F. Lista and F. Arduini, *Biosens. Bioelectron.*, 2021, **171**, 112686.
80 E. Martínez-Periñán, T. Garcia-Mendiola, E. Enebral-Romero, R. Del Cano, M. Vera-Hidalgo, M. Vazquez Sulleiro, C. Navio, F. Pariente, E. M. Perez and E. Lorenzo, *Biosens. Bioelectron.*, 2021, **189**, 113375.
81 H. Chen, J. Huang, A. Palaniappan, Y. Wang, B. Liedberg, M. Platt and A. I. Tok, *Analyst*, 2016, **141**, 2335–2346.
82 Y. Wu, R. D. Tilley and J. J. Gooding, *J. Am. Chem. Soc.*, 2019, **141**, 1162–1170.
83 F. Curti, S. Fortunati, W. Knoll, M. Giannetto, R. Corradini, A. Bertucci and M. Careri, *ACS Appl. Mater. Interfaces*, 2022, **14**, 19204–19211.
84 J. Kwon, Y. Lee, T. Lee and J. H. Ahn, *Anal. Chem.*, 2020, **92**, 5524–5531.
85 J. McClements, L. Bar, P. Singla, F. Canfarotta, A. Thomson, J. Czulak, R. E. Johnson, R. D. Crapnell, C. E. Banks, B. Payne, S. Seyedin, P. Losada-Perez and M. Peeters, *ACS Sens.*, 2022, **7**, 1122–1131.
86 Q. Zhou, Y. Sasaki, K. Ohshiro, H. Fan, V. Montagna, C. Gonzato, K. Haupt and T. Minami, *J. Mater. Chem. B*, 2022, **10**, 6808–6815.
87 W. Gao, S. Emaminejad, H. Y. Y. Nyein, S. Challa, K. Chen, A. Peck, H. M. Fahad, H. Ota, H. Shiraki, D. Kiriya, D. H. Lien, G. A. Brooks, R. W. Davis and A. Javey, *Nature*, 2016, **529**, 509–514.
88 D. Gosselin, M. Gougis, M. Baque, F. P. Navarro, M. N. Belgacem, D. Chaussy, A. G. Bourdat, P. Mailley and J. Berthier, *Anal. Chem.*, 2017, **89**, 10124–10128.
89 M. Zea, R. Texido, R. Villa, S. Borros and G. Gabriel, *ACS Appl. Mater. Interfaces*, 2021, **13**, 33524–33535.
90 B. M. Hryniewicz, J. Volpe, L. Bach-Toledo, K. C. Kurpel, A. E. Deller, A. L. Soares, J. M. Nardin, L. F. Marchesi, F. F. Simas, C. C. Oliveira, L. Huergo, D. E. P. Souto and M. Vidotti, *Mater. Today Chem.*, 2022, **24**, 100817.
91 J. Jiao, J. Zuo, H. Pang, L. Tan, T. Chen and H. Ma, *J. Electroanal. Chem.*, 2018, **827**, 103–111.
92 V. Gautam, K. P. Singh and V. L. Yadav, *Carbohydr. Polym.*, 2018, **189**, 218–228.
93 D. Jemmeli, E. Marcoccio, D. Moscone, C. Dridi and F. Arduini, *Talanta*, 2020, **216**, 120924.
94 V. Mazzaracchio, A. Serani, L. Fiore, D. Moscone and F. Arduini, *Electrochim. Acta*, 2021, **394**, 139050.
95 X. Liang, H. Li, J. Dou, Q. Wang, W. He, C. Wang, D. Li, J. M. Lin and Y. Zhang, *Adv. Mater.*, 2020, **32**, 2000165.
96 H. Huang, Y. Li, S. Chen, Z. Liu, Y. Cui, H. Li, Z. Guo and X. Huang, *Anal. Chim. Acta*, 2022, **1189**, 339208.
97 J. M. Mohan, K. Amreen, M. B. Kulkarni, A. Javed, S. K. Dubey and S. Goel, *Colloids Surf., B*, 2021, **208**, 112056.
98 M. Jozghorbani, M. Fathi, S. H. Kazemi and N. Alinejadian, *Anal. Biochem.*, 2021, **613**, 114017.
99 R. Campos, J. Borme, J. R. Guerreiro, G. Machado, M. F. Cerqueira, D. Y. Petrovykh and P. Alpuim, *ACS Sens.*, 2019, **4**, 286–293.
100 M. Lu, Y. Deng, Y. Luo, J. Lv, T. Li, J. Xu, S.-W. Chen and J. Wang, *Anal. Chem.*, 2019, **91**, 888–895.
101 J. Li, L. Zhao, W. Wang, Y. Liu, H. Yang, J. Kong and F. Si, *Sens. Actuators, B*, 2021, **328**, 129031.
102 Y. Fang, Q. Hu, X. Yu and L. Wang, *Sens. Actuators, B*, 2018, **258**, 238–245.
103 Y. Wang and G. J. Weng, in *Micromechanics and Nanomechanics of Composite Solids*, ed. S. A. Meguid and G. J. Weng, Springer International Publishing, Cham, 2018, pp. 123–156.
104 T. A. Yemata, Q. Ye, H. Zhou, A. K. K. Kyaw, W. S. Chin and J. Xu, in *Hybrid Polymer Composite Materials*, ed. V. K. Thakur, M. K. Thakur and A. Pappu, Woodhead Publishing, 2017, pp. 169–195.
105 J. Phiri, P. Gane and T. C. Maloney, *Mater. Sci. Eng., B*, 2017, **215**, 9–28.
106 F. Otero and E. Magner, *Sensors*, 2020, **20**, 3561.
107 M. M. Rahman, M. G. Ara, M. A. Alim, M. S. Uddin, A. Najda, G. M. Albadrani, A. A. Sayed, S. A. Mousa and M. M. Abdel-Daim, *Int. J. Mol. Sci.*, 2021, **22**, 4498.

108 Y. Hernandez, V. Nicolosi, M. Lotya, F. M. Blighe, Z. Sun, S. De, I. T. McGovern, B. Holland, M. Byrne, Y. K. Gun'Ko, J. J. Boland, P. Niraj, G. Duesberg, S. Krishnamurthy, R. Goodhue, J. Hutchison, V. Scardaci, A. C. Ferrari and J. N. Coleman, *Nat. Nanotechnol.*, 2008, **3**, 563–568.
109 X. Xi, D. Wu, L. Han, Y. Yu, Y. Su, W. Tang and R. Liu, *ACS Nano*, 2018, **12**, 5436–5444.
110 B. Wei, K. Mao, N. Liu, M. Zhang and Z. Yang, *Biosens. Bioelectron.*, 2018, **121**, 41–46.
111 C. B. Breslin, D. Branagan and L. M. Garry, *J. Appl. Electrochem.*, 2019, **49**, 195–205.
112 E. Buber, M. Kesik, S. Soylemez and L. Toppare, *J. Electroanal. Chem.*, 2017, **799**, 370–376.
113 S. Xu, Y. Zhang, Y. Zhu, J. Wu, K. Li, G. Lin, X. Li, R. Liu, X. Liu and C.-P. Wong, *Biosens. Bioelectron.*, 2019, **135**, 153–159.
114 Y. Zhang, G. I. N. Waterhouse, Z.-p. Xiang, J. Che, C. Chen and W. Sun, *Food Chem.*, 2020, **326**, 126976.
115 Q. Li, J. Zhao, Y. Huang, W. Tang and X. Guo, *IEEE Sens. Lett.*, 2018, **2**, 1–4.
116 X. T. Liu, Y. L. Guo, Y. Q. Ma, H. J. Chen, Z. P. Mao, H. L. Wang, G. Yu and Y. Q. Liu, *Adv. Mater.*, 2014, **26**, 3631–3636.
117 J. Lee, M. J. Panzer, Y. He, T. P. Lodge and C. D. Frisbie, *J. Am. Chem. Soc.*, 2007, **129**, 4532–4533.
118 J. Smith, R. Hamilton, I. McCulloch, N. Stingelin-Stutzmann, M. Heeney, D. D. C. Bradley and T. D. Anthopoulos, *J. Mater. Chem.*, 2010, **20**, 2562–2574.
119 K. Zhao, O. Wodo, D. Ren, H. U. Khan, M. R. Niazi, H. Hu, M. Abdelsamie, R. Li, E. Q. Li, L. Yu, B. Yan, M. M. Payne, J. Smith, J. E. Anthony, T. D. Anthopoulos, S. T. Thoroddsen, B. Ganapathysubramanian and A. Amassian, *Adv. Funct. Mater.*, 2016, **26**, 1737–1746.
120 R. Hamilton, J. Smith, S. Ogier, M. Heeney, J. E. Anthony, I. McCulloch, J. Veres, D. D. C. Bradley and T. D. Anthopoulos, *Adv. Mater.*, 2009, **21**, 1166–1171.
121 L. Feng, W. Tang, X. Xu, Q. Cui and X. Guo, *IEEE Electron Device Lett.*, 2013, **34**, 129–131.
122 W. Tang, L. Feng, P. Yu, J. Zhao and X. Guo, *Adv. Electron. Mater.*, 2016, **2**, 1500454.
123 L. Feng, W. Tang, X. Xu, Q. Cui and X. Guo, *IEEE Electron Device Lett.*, 2012, **34**, 129–131.
124 W. Tang, L. Feng, P. Yu, J. Zhao and X. Guo, *Adv. Electron. Mater.*, 2016, **2**, 1500454.
125 C. Jiang, H. W. Choi, X. Cheng, H. B. Ma, D. Hasko and A. Nathan, *Science*, 2019, **363**, 719–723.
126 J. Zhao, W. Tang, Q. Li, W. Liu and X. Guo, *IEEE Electron Device Lett.*, 2017, **38**, 1465–1468.
127 D. H. Kim, B. L. Lee, H. Moon, H. M. Kang, E. J. Jeong, J. I. Park, K. M. Han, S. Lee, B. W. Yoo, B. W. Koo, J. Y. Kim, W. H. Lee, K. Cho, H. A. Becerril and Z. Bao, *J. Am. Chem. Soc.*, 2009, **131**, 6124–6132.
128 J. Lee, J. W. Chung, G. B. Yoon, M. H. Lee, D. H. Kim, J. Park, J. K. Lee and M. S. Kang, *ACS Appl. Mater. Interfaces*, 2016, **8**, 30344–30350.
129 X. Jia, C. Fuentes-Hernandez, C. Y. Wang, Y. Park and B. Kippelen, *Sci. Adv.*, 2018, **4**, eaao1705.
130 W. Tang, J. Zhao, Y. Huang, L. Ding, Q. Li, J. Li, P. You, F. Yan and X. Guo, *IEEE Electron Device Lett.*, 2017, **38**, 748–751.
131 J. Zhao, Q. Li, Y. Huang, S. Li, W. Tang, S. Peng, S. Chen, W. Liu and X. Guo, presented in part at the 2017 IEEE Int. Electron Devices Meeting (IEDM), 2017, pp. 8.3.1–8.3.4.
132 T. Minami, T. Minamiki and S. Tokito, *Jpn. J. Appl. Phys.*, 2016, **55**, 04EL02.
133 T. Minami, Y. Sasaki, T. Minamiki, S. I. Wakida, R. Kurita, O. Niwa and S. Tokito, *Biosens. Bioelectron.*, 2016, **81**, 87–91.
134 R. Mitobe, Y. Sasaki, W. Tang, Q. Zhou, X. Lyu, K. Ohshiro, M. Kamiko and T. Minami, *ACS Appl. Mater. Interfaces*, 2022, **14**, 22903–22911.
135 T. Minami, T. Minamiki and S. Tokito, *Chem. Lett.*, 2016, **45**, 371–373.
136 T. Minami, T. Sato, T. Minamiki and S. Tokito, *Anal. Sci.*, 2015, **31**, 721–724.
137 T. Minamiki, Y. Sasaki, S. Tokito and T. Minami, *ChemistryOpen*, 2017, **6**, 472–475.
138 R. Shiwaku, H. Matsui, K. Nagamine, M. Uematsu, T. Mano, Y. Maruyama, A. Nomura, K. Tsuchiya, K. Hayasaka, Y. Takeda, T. Fukuda, D. Kumaki and S. Tokito, *Sci. Rep.*, 2018, **8**, 6368.
139 T. Minami, T. Minamiki, Y. Hashima, D. Yokoyama, T. Sekine, K. Fukuda, D. Kumaki and S. Tokito, *Chem. Commun.*, 2014, **50**, 15613–15615.
140 K. Nagamine, T. Mano, R. Shiwaku, H. Furusawa, H. Matsui, D. Kumaki and S. Tokito, *Sens. Mater.*, 2019, **31**, 1205–1213.
141 J. Song, J. Dailey, H. Li, H. J. Jang, P. Zhang, J. T. Wang, A. D. Everett and H. E. Katz, *Adv. Funct. Mater.*, 2017, **27**, 1606506.
142 T. Minamiki, T. Minami, Y. Sasaki, R. Kurita, O. Niwa, S. Wakida and S. Tokito, *Anal. Sci.*, 2015, **31**, 725–728.
143 T. Minamiki, T. Minami, R. Kurita, O. Niwa, S.-i. Wakida, K. Fukuda, D. Kumaki and S. Tokito, *Appl. Phys. Lett.*, 2014, **104**, 243703.
144 B. Ouyang, Y. Song, W. Cai, Y. Tang, Y. Si, X. Yin, S. Chen, W. Tang, H. Zhou, B. Huang and X. Guo, presented in part at the 2021 IEEE Int. Electron Devices Meeting (IEDM), 2021, pp. 16.3.1–16.3.4.
145 N. Verma, Y. Hu, L. Huang, W. S. Rieutort-Louis, J. S. Robinson, T. Moy, B. Glisic, S. Wagner and J. C. Sturm, *Proc. IEEE*, 2015, **103**, 690–712.
146 G. Whiting, D. Schwartz, T. Ng, B. Krusor, R. Krivacic, A. Pierre, A. Arias, M. Härting, D. Van Buren and K. Short, *Flexible Printed Electron.*, 2017, **2**, 034002.
147 T. Sekitani, T. Yokota, K. Kuribara, M. Kaltenbrunner, T. Fukushima, Y. Inoue, M. Sekino, T. Isoyama, Y. Abe and H. Onodera, *Nat. Commun.*, 2016, **7**, 1–11.
148 L. Feng, W. Tang, J. Zhao, R. Yang, W. Hu, Q. Li, R. Wang and X. Guo, *Sci. Rep.*, 2016, **6**, 20671.

149 S. Qiu, Y. Yu, X. Guo, W. Tang, X. Xi, W. Sun, Y. Huang, R. Liu, Y. Su, L. Jiang and Q. Wei, *IEEE Sens. Lett.*, 2018, **2**, 1–4.
150 S. F. Berlanda, M. Breitfeld, C. L. Dietsche and P. S. Dittrich, *Anal. Chem.*, 2021, **93**, 311–331.
151 R. Vinoth, T. Nakagawa, J. Mathiyarasu and A. M. V. Mohan, *ACS Sens.*, 2021, **6**, 1174–1186.
152 Z. Liao, J. Wang, P. Zhang, Y. Zhang, Y. Miao, S. Gao, Y. Deng and L. Geng, *Biosens. Bioelectron.*, 2018, **121**, 272–280.